C.P. No. 1179

C.P. No. 1179

MINISTRY OF AVIATION SUPPLY

AERONAUTICAL RESEARCH COUNCIL

CURRENT PAPERS

THE PERFORMANCE OF AXIAL-FLOW COMPRESSORS OF DIFFERING BLADE ASPECT RATIO

By

G.T.S. Fahmi

Department of Mechanical Engineering, University of Liverpool

LONDON : HER MAJESTY'S STATIONERY OFFICE

1971

PRICE 95p NET

CP No. 1179**
August 1968

THE PERFORMANCE OF TWO AXIAL-FLOW COMPRESSORS OF DIFFERING BLADE ASPECT RATIO

-by-

G. J. S. Fahmi*

SUMMARY

The performance of axial-flow compressors is known to be adversely affected by increasing the aspect ratio (the ratio of blade height to chord length).

Experimental investigations have been carried out on a single-stage, low speed axial-flow compressor with a parallel annulus and a hub-tip ratio of 0.750. The tests were conducted at two blade aspect ratios; one and two. The Reynolds number was held constant at 1.9×10^5 by testing each aspect ratio at different speeds. The tip clearances and blade row axial spacing at the inner diameter were kept identical for both aspect ratios.

The overall performance characteristics show that the compressor of aspect ratio 1 has a wider range of operation and in general a higher static pressure rise than that for the compressor of aspect ratio 2.

Traverses show that the three-dimensional flow outside the wall boundary layers is substantially the same for both aspect ratios. They also show that the major aspect ratio effect is caused by wall stall which occurs at the blade ends. The compressor of aspect ratio 2 is seen to be more severely affected by this stall than that of aspect ratio 1. Practically no difference in the work done was evident between the different aspect ratios. It is concluded that the adverse effect of increasing the blade row aspect ratio on the performance of axial-flow compressor stages is caused by wall stall.

A three-dimensional flow calculation, including profile, secondary and clearance losses and secondary distortion of flow angles, is described.

CONTENTS/

---

* Lecturer at Engineering College, Baghdad University, Iraq.

** Replaces A.R.C.31 818

CONTENTS

APPENDICES

1. INTRODUCTION

An increase in aspect ratio (the ratio of blade length to chord) has been observed to have an adverse effect on the performance of single-stage and multi-stage axial flow compressors.

Experimental investigations which led to such an observation have been made by a number of research workers. The most recent of these has been the work of Horlock et al[1], Pollard[2], and Shaalan[3] on compressor cascades, and of Figg[4], in parallel with the author, on axial flow compressors. A review on past and recent work is given in Ref.5.

The object of the present work is an experimental study of the effect of blade aspect ratio on the performance of axial flow compressors. In order to do this a single stage, low speed, large axial flow compressor was used. The stage consisted of three blade rows (i.g.v., rotor and stator), each having hub-tip ratio of 0.750.

Identical blading of exponential design (see Ref.13) and aspect ratios 1.0 and 2.0 were tested, the aspect ratio of all three blade rows being kept the same. The experimental programme consisted of testing each of the aspect ratios at the same blade Reynolds number and over a wide range of mass flows. The Reynolds number was kept constant by changing the r.p.m. Detailed traverses were taken behind each blade row in order to study the flow conditions.

A theoretical treatment of the problem based on the actuator disc method of calculation has been carried in two steps. The first of these is reported in Ref.6, in which the flow is considered to be three-dimensional, axi-symmetric, incompressible and inviscid. The second step is reported in the present work*. The same problem is considered but with total pressure losses, tip clearance, secondary flows and changes in outlet air angle due to the turning of non-uniform flow through blade row passages, all accounted for.

Results of the actuator disc calculations (including losses) which have been made for the single-stage compressor of hub-tip 0.750 are compared with the experimental traverses.

2. APPARATUS AND EXPERIMENTAL METHODS

2.1 The axial-flow compressor

The axial-flow compressor rig used in the experiments is shown on Plate 1. The compressor without the blading consists of a rotor surrounded by a stator casing, a diffuser and a throttle. It is driven by a 32 H.P. induction motor through an eddy current coupling and V-belts which pass through the diffuser. The rotor, which is three feet in diameter, and the stator, which has an inside diameter of four feet, are fabricated in mild steel and form a cylindrical annular passage with no hub or tip curvature. Maximum rotor speed is 1000 r.p.m..

The air is drawn through an annular intake duct made in fibreglass reinforced polyester resin whose form is shown in Fig.1. This form of ducting reduces upstream disturbances and provides a uniform type of axial velocity profile upstream of the first row of blades.

The/

---

* Appendix B

The diffuser has an inner-cone made in timber and plywood whilst the octagonal outer-wall is made in timber and Masonite board. The flow is controlled by the exit throttle which consists of 20 gauge sheet steel covering a frame of mild steel rods.

The compressor consists of three rows of blades (guide vanes, rotor, stator) and a full description is given in Ref.7.

2.2 Pressure tappings and traversing mechanism

Five static pressure tappings were equally spaced around the circumference of the compressor inner and outer walls at several axial locations, Fig.2. Full radial and circumferential traversing over at least one blade pitch, Fig.3, is allowed by circumferential slots (5/8 ins. wide), cut in the stator casing.

2.3 Instrumentation and calibrations

In examining aspect ratio effects on axial-flow compressor performance experimentally, emphasis was centred upon the measurement of axial velocity profiles at the trailing edges of the blade rows, under a variety of flow conditions. Such measurements must be carried out within the small axial clearance, normally less than 0.500 ins, between neighbouring blade rows. This required an instrument small in dimensions but robust in construction, reading yaw angle, total and static pressures simultaneously. Such requirements were satisfied by a combination probe of the wedge type (Plate II and Fig.4). The accuracy of this type of instrument is discussed in Ref.8.

Fig.4 shows the wedge probe detail.

Calibration of the wedge for total head was carried out in the working section of a low speed, large cascade wind tunnel that could provide flow speeds up to 70 feet per second. Dynamic head readings from the wedge, set at its reference angle, were then compared with the true readings obtained from an NPL pitot-static instrument placed in the vicinity of the wedge. The ratio of the true dynamic head to actual dynamic head reading then gives the total head calibration factor. Fig.5 shows the calibration curve.

A check on the turbulence level effects on the total head and yaw readings recorded by the wedge was obtained by placing various turbulence grids, generating turbulences in the free stream varying from 0.5% to 10%, upstream of the working section of the wind tunnel. The results, which indicate no effect of turbulence, are shown in Fig.5.

The compressor rotational speed was recorded via a voltage pulse generator driven by the eddy current coupling shaft, and connected to an Avo-meter functioning as a voltmeter. The Avo-meter was calibrated against a revolution counter over the whole speed range of the compressor.

All the pressures recorded by the instruments or by the wall tappings were measured on an inclined multi-tube (alcohol) manometer.

3./

3. EXPERIMENTAL INVESTIGATIONS*

3.1 Overall performance characteristics

Curves of overall static pressure rise coefficient $\frac{\Delta p_{overall}}{\frac{1}{2}\rho U_m^2}$ versus flow coefficient $\frac{c_{x,o}}{U_m}$ are shown in Fig.9, for each of the two aspect ratios, where $\overline{c}_{x,o}$ and $\overline{\Delta p}_{o,a}$ are calculated from mean values of 10 circumferential wall static pressure readings. The plot is shown for a wide range of flow coefficients (from 1.2 to 0.4 of the design value), and for several Reynolds numbers (Re = 1.9×10^5, 1.45×10^5, 0.87×10^5 for AR = 2; Re = 1.9×10^5, 1.16×10^5 for AR = 1).

At each Reynolds number the throttle was set fully open. It was then closed progressively to the stall point, considerable care being taken to obtain readings at the points just prior to stall, and immediately after stall. A sudden fall in the static pressure rise across the compressor occurred at the onset of stall, and under such a condition it proved quite impossible to operate the compressor at an intermediate point. The stall onset lines are therefore shown dotted on Fig.9. The audible detection of stall was confirmed by observation of oscillations of the fluid in the manometer tubes connected to the five circumferential static pressure wall tappings.

When the throttle was opened progressively from stalled through to unstalled operation, it was apparent that the behaviour on throttle opening was different from that for throttle closing since the static pressure rise for unstalled operation was different in each case. The operation line for throttle opening is also shown dotted on Fig.9.

3.2 Entry conditions

Using the wedge instrument, radial traverses were made at entry to the stage. Readings in the inner and outer wall boundary layer were taken at 0.025" intervals from the wall for the first 0.250 of an inch and then at 0.100" intervals for the next 0.750 of an inch. Mainstream readings were taken at 1" intervals. Axial velocity, inlet flow angle, static and total pressures thus obtained are shown plotted against radius on Figs.10 and 11 for aspect ratio 2 and 1 respectively. The flow coefficients at which these traverses were made are ϕ = 0.647, 0.527 and 0.427. The reason for choosing these values is given in the next section. For purposes of clarity only selected measurement points are shown plotted on Figs.10 and 11.

Entry conditions and in particular the boundary layers at entry appear to be similar for both aspect ratios. The boundary layer thickness deduced from total pressure measurements was slightly greater at the outer annulus wall than at the inner annulus wall for both cases.

3.3/

---

* The compressor stage with aspect ratio 1 blades and that with aspect ratio 2 blades is hereafter referred to as compressor 1 and compressor 2 respectively.

3.3 Blade row traverses

Using the wedge instrument, circumferential traverses over one blade pitch, at 1" intervals along the blade height and behind each blade row were conducted. Trailing edge mean values of axial velocity, outlet flow angle, static pressure and total pressure loss coefficient calculated from these circumferential measurements are shown plotted against radius* for three flow coefficients ($\phi = 0.647$, 0.527, 0.427) and for each aspect ratio on Figs.12 to 22. The dotted lines on Figs.12 to 17 represent readings obtained in the end wall boundary layer where high accuracy cannot be expected.

The choice of the three flow coefficients at which all traverses have been carried out was based on the consideration that much of the unstalled mass flow range is bounded by the highest and lowest flow coefficients. The highest flow coefficient, $\phi = 0.647$, represented a condition where incidences are negative and compressor loadings are low. The second flow coefficient, $\phi = 0.527$, represented design conditions where incidences are near nominal and total pressure losses are minimum. The lowest flow coefficient, $\phi = 0.427$, represented near-stall conditions.

Although the lowest flow condition, $\phi = 0.427$, may not be as "near to stall" for compressor 1 as for compressor 2 , it was thought logical to test both compressors at the same value of flow coefficient.

3.4 Total pressure traverses

The measurement of total pressure may, in general, be regarded as more reliable than that of static pressure and yaw angle. In order that this measurement might be carried out in the boundary layer region near the annulus walls, the wedge instrument, functioning as a pitot tube, was used. The other function of the wedge instrument, namely flow direction measurement, was also employed but only in an approximate way** so as to ensure that the wedge pitot tube was directed towards the flow to within ±5°.

The total pressure measurements are presented on a non-dimensional basis and in contour form in Figs.23 to 28 for values of ϕ of 0.527 and 0.427.

3.5 Comparison with calculated results

Full calculations of the flow, including allowances for profile and secondary losses and changes in angles due to secondary flow were made for both compressors 1 and 2 for values of flow coefficient corresponding to the experimental results.

Details of these calculations are given in Appendix B.

The results of the calculations are compared with corresponding experimental measurements in Figs.12 to 17.

4./

---

* The method of calculation of experimental results is given in Ref.5.

** The normal manner in which the flow total head and direction is measured by the wedge instrument is to rotate the instrument until the readings recorded by the two wedge static holes are exactly equal.

4. DISCUSSION

4.1 Overall characteristics

The overall characteristics for the compressors 1 and 2, (Fig.9) show quite clearly that compressor 1 has a superior unstalled mass flow range. It also has a superior peak pressure rise. A close study of the two performance curves shows that the increase in range and static pressure rise is quite substantial. The increase is approximately 18% for the former and 10% for the latter.

At flow coefficients higher than design (i.e., at $\phi > 0.527$), the performance of both compressors appears to be identical. At flow coefficients lower than design differences in performance may be seen to increase and just before stall these differences became maximum.

It is of interest to note that as the flow coefficient decreases, the compressor 1 performance curve levels off as it reaches the peak and then drops a little before it finally goes into stall. The compressor 2 performance curve, on the other hand, appears to reach its peak and then goes into stall just before it levels off. This suggests that compressor 1 approaches stall more stably than compressor 2.

In the stall region, static pressure readings recorded on the alcohol manometer oscillate so that these readings cannot be considered accurate. However, the two compressors exhibit hysteresis loops of the same general shape, the loop for compressor 1 being the larger of the two. The static pressure rise in the stall region for compressor 1 appears to maintain the superiority over the static pressure rise for compressor 2, exhibited prior to stall.

No noticeable Reynolds number effects can be observed on either curve.

4.2 Axial velocity profiles in the mainstream

The axial velocity profiles behind any one blade row of compressor 1 do not show any appreciable difference from the profiles behind the corresponding blade row of compressor 2, Figs.12, 13 and 14. This seems particularly true at the design and higher than design flow coefficients (i.e., $\phi = 0.527$ and 0.647). At the low flow coefficient, $\phi = 0.427$, slight differences between compressor 1 and 2 mainstream axial velocities may be detected, the values for compressor 1 being the lower of the two. This implies thicker annulus wall boundary layers for compressor 2.

4.3 Air outlet angles

The air outlet angles at the trailing edge of i.g.v., rotor and stator blade rows are shown on Figs.15, 16 and 17 for both compressors 1 and 2.

No appreciable differences in the mainstream values of outlet angle between compressor 1 and 2 can be observed. Angle measurements in the flow regions near the annulus walls are shown as a dotted line.

4.4 Static pressures

The static pressures at the trailing edges of i.g.v., rotor and stator, shown on Figs.18, 19 and 20 for both compressors 1 and 2 do not show any conclusive differences. (The accuracy of the mainstream measurements is checked against a static wall tapping reading at each flow coefficient investigated. The results show that the agreement between the static pressures recorded by the wedge instrument and by the wall tapping is quite good.)

4.5/

4.5 Total pressure losses

The relative total pressure loss coefficient for the rotor of compressor 2 shows a considerable difference from that for the compressor 1 rotor, Fig.21. This difference appears as an increase in the loss coefficient near the root section for compressor 2, as the flow coefficient is decreased, no such increase being observed for compressor 1. This seems to suggest that stall is taking place in the region near the inner annulus wall, (i.e., the region where the rotor blade meets the inner annulus wall), for compressor 2, but not for compressor 1.

At $\phi = 0.647$ and 0.527, the absolute total pressure loss coefficient is very much the same across the stator of compressor 1 and 2, Fig.22. At $\phi = 0.427$, the stator of compressor 2 shows clearly a region of high loss extending from the inner annulus wall to mid-span. The stator of compressor 1, on the other hand, shows that this loss is more confined to the annulus wall region. This suggests that at this low flow coefficient, the stator of compressor 2 is suffering from stall over the lower part of its span whilst the stator of compressor 1 is suffering from a much less spread stall.

4.6 Total pressure contours

As a result of the somewhat inconclusive differences shown in the results of the experimental investigations discussed in the previous sections, it became evident that if any conclusions on the effect of aspect ratio were to be drawn, traverses extending in the annulus wall boundary layer had to be undertaken.

Complete total pressure contours at exit from the three blade rows are shown for compressors 1 and 2 operating under design ($\phi = 0.527$) and off-design conditions ($\phi = 0.427$), on Figs.23 to 28.

At the trailing edge of the i.g.v. blade row the waviness of the "mid-wake" line at the low flow condition for compressor 2 indicates that secondary flow is stronger in compressor 2 than compressor 1, although the boundary layer thickness on the annulus walls for both flow conditions appears to be much the same for both aspect ratios.

The total pressure contours measured behind the rotor blade row are experimental mean values of the true time-varying quantities. A very high degree of accuracy is therefore not to be expected, but nevertheless the results, Figs.24 and 27, exhibit significant features and show some particular differences between the two compressors.

At $\phi = 0.527$, the general level of total pressure at this section is slightly higher in compressor 1 than in compressor 2. At $\phi = 0.427$, this difference is accentuated and the results for both compressors indicate regions of higher total pressure at the extreme ends of the blade span. However, the trough in total pressure over the part of the blade near the hub is much more marked for compressor 2 than for compressor 1.

The explanation of these results is not easy to find. The measurements of relative air angles, Fig.16, do not extend into the root region in which the higher values of total pressure are observed. The higher values may be associated with over-turning at the root, or with an increase in work done as a result of reduced axial velocity in the end wall boundary layers.

Certainly there are marked differences between the total pressure distributions downstream of the two rotors but the present experimental measurements are not sufficiently detailed to indicate the cause of the difference.

The total pressure contours at the trailing edge of the stator blade row also show substantial differences between compressors 1 and 2. At $\phi = 0.527$, the annulus wall boundary layer thickness is evidently thicker for compressor 2 than for compressor 1, although the boundary layer thicknesses on the suction surface of the blades in the mainstream is very much the same for both compressors. At $\phi = 0.427$, major differences are apparent, complete wall stall occurring in compressor 2, particularly at the hub, but not in compressor 1. This result reflects the total pressure loss coefficient results obtained for the stator, Fig.22, and may result from variation of incidence on to the stator blades associated with the total pressure distribution at the rotor outlet.

4.7 Flow calculation with losses

Actuator disc calculations (including losses) of the trailing edge axial velocity profiles, Figs.12, 13 and 14, show good agreement with experiment over most of the blade height. In general, any disagreement appears to be in the regions near the inner and outer annulus walls. Neither the losses nor the outlet angles, Figs.15, 16 and 17, near the annulus walls can be estimated with sufficient accuracy.

There are two factors that may be considered responsible for incorrectly estimating the profiles near the annulus walls. First, the use of cascade loss data is open to question, as may be seen by comparing the curves of Fig.8 (the loss distributions used in the calculations) with those of Figs.21 and 22 (the loss distributions actually measured).

In spite of these disparities, the use of cascade data in expressing the loss for the middle part of a blade operating near its design conditions, results in a reasonably accurate prediction of performance, but even the inclusion of distributed secondary and clearance losses, as in the present calculation, does not lead to very good estimates of the flow at the annulus walls.

Secondly, the assumptions made on the size and growth of the annulus wall boundary layer are critical in the loss and angle calculations. The thickness of the boundary layers at root and tip that were actually used in the loss calculations were deduced from early traverses at the tip section and were approximately one inch. The entry velocity profile assumed for the calculations is shown on Fig.6 together with the measured profile. It is evident from Fig.6 that the profile assumed for the calculation at the inner annulus wall is substantially in error, and the calculation of the profiles at the inner wall is invalidated.

5. CONCLUSIONS

5.1 The overall performance characteristics have shown that the range of unstalled operation for compressor 1 is wider than that for compressor 2. At flow coefficients higher than design, the performance of both compressors appears to be identical. At flow coefficients lower than design, differences in performance appear, with compressor 1 achieving the higher overall static pressure rise. Stall with compressor 2 seems to occur suddenly whilst it is gradual with compressor 1.

5.2 The traverse results show that the three-dimensional mainstream flow is substantially the same for both compressors, thus confirming the inviscid calculations of Ref.6.

5.3/

5.3 The major cause of the difference in the overall performance of the two compressors appears to be the marked differences between the total pressure distributions downstream of the rotor at the same (near-stall) flow coefficient. In addition, there is severe stator wall stall in compressor 2, compared with very little stator wall stall in compressor 1.

5.4 Since no appreciable difference in the values of trailing edge axial velocity and outlet air angle has been observed between compressors 1 and 2, it is concluded that the work done by both compressors over the whole flow range is substantially the same.

5.5 Comparison of the actuator disc "loss" calculations with experimental results, Ref.5, shows that while some improvement on inviscid calculations is achieved, the velocity profiles, particularly at the hub and the annulus walls still cannot be predicted accurately. This is due to the inadequacy of the loss data and poor estimates of annulus wall boundary layer thickness.

ACKNOWLEDGEMENTS

The author wishes to express his gratitude to Professor J. H. Horlock for the guidance under which this work was carried out, and to Professor J. F. Norbury for editing the manuscript.

APPENDIX A /

APPENDIX A

A.1 Blade Design (aspect ratio 1, 2)

The 'exponential' method of design was chosen. The tangential velocity 'c_θ' is given by

$$
\begin{aligned}
c_{\theta,1} &= a + \frac{b}{R} \quad \text{downstream of rotor} \\
c_{\theta,2} &= a - \frac{b}{R} \quad \text{downstream of stator}
\end{aligned}
\qquad \ldots(A.1)
$$

where a, b are constants.

To design the blade, it is necessary to specify values of space-chord ratio and design incidence at the particular radial locations. The experimental work on compressor cascades carried out in the Mechanical Engineering Department at Liverpool University was conducted on blades of C4 profile, 30° camber, 36° stagger, giving blade inlet and outlet angles of 51° and 21° respectively. The design incidence and the space-chord ratio being 1°50' and 0.875 respectively. For the design of exponential blades, it was thought desirable that the above design data should be adopted for the mean sections of rotor and stator (i.e., 5070 reaction was selected). The rotor or stator blade then had a mean section of profile, camber stagger and space-chord ratio similar to those for the cascade. Furthermore, the design incidence on the blade was selected to be 1°50' all along the blade height.

With the space-chord ratio chosen, the number of blades in each blade row and for each aspect-ratio can be determined. Thus, the number of blades per row is 25 and 50 for aspect-ratio 1 and 2 respectively.

The Reynolds number (based on the rotor blade mean section speed and the blade chord, i.e., $Re = \frac{U_m . C}{\nu}$) depends on the maximum power obtainable from the compressor motor and hence the maximum rotational speed. To vary the blade aspect ratio and keep the Reynolds number constant requires that the rotor rotational speed be varied proportionally. Re was chosen to be equal to $1.9 \times 10^{+5}$ and the design rotational speeds were 312.5 and 625 r.p.m. for aspect ratio 1 and 2 respectively.

The i.g.v. geometry was chosen in a similar fashion except that the stagger was set at -20°, and the incidence was -5°*.

With $c_{\theta,1,m}$ and $c_{\theta,2,m}$ specified from the velocity triangles, the constants a and b may now be deduced from equations (A.1).

The/

---

* The twist along the i.g.v. blade height is centred along its leading edge. The twist along the rotor and stator blade height is centred along the mid-chord line.

The air angle distributions with radius may then be obtained by considering the radial equilibrium equations at the design point, where there are no gradients of stagnation enthalpy, i.e., equal work being done at all radii, thus,

$$c_x \frac{dc_x}{dr} + \frac{c_\theta}{r} \cdot \frac{d}{dr}(r.c_\theta) = 0 \qquad \ldots(A.2)$$

Integrating equation (A.2) with respect to r, we get

$$c_x^2 = \text{constant} - 2a^2 . \log_e R \pm (b/aR)(1 - R) \qquad \ldots(A.3)$$

where the constant is determined by satisfying the continuity condition.

Using the actuator disc theory these "infinity" axial velocities obtained from eqn. (A.3), may be modified to give the leading and trailing edge values by allowing for the interference effects of the adjacent blade rows.

With the blade axial spacing, the blade chordal dimension and the hub-tip ratio of the compressor all specified, each blade row may then be replaced by a hypothetical actuator disc located at the blade centre line (mid-chord), Ref.9.

The trailing edge axial velocities could now be calculated from interference equations of the form

$$c_{x,ie} = c_{x,i} - \frac{(c_{x,i} - c_{x,i-1})e^{-\frac{\pi X}{L}}}{2} + \frac{(c_{x,i+1} - c_{x,i})e^{-\frac{\pi X}{L}}}{2} \qquad \ldots(A.4)$$

allowing for interference effects from adjacent disc only, Ref.10.

The design air angles distribution with radius are then deduced from

$$\tan \alpha_e = \frac{c_{\theta,1}}{c_{x,1e}} = \frac{a - \frac{b}{R}}{c_{x,1e}} \quad \text{for a rotor}$$

$$\ldots(A.5)$$

$$\tan \beta_e = \frac{U - c_{\theta,1}}{c_{x,1e}} = \frac{U - (a + \frac{b}{R})}{c_{x,1e}} \quad \text{for a stator}$$

Ref.11 gives detailed application of actuator disc theory to design of axial compressors.

Blade angles, camber and stagger at various radial positions may now be computed for a blade that will produce such air angle distributions. This computation follows an iterative procedure whereby deviation rules and other empirical cascade data for deflection are employed, Ref.12. Such a procedure is lengthy and a computer programme was devised for the purpose of speeding up the calculations.

The/

The final step of blade design, once a profile shape is decided upon, is the computation of the blade surface co-ordinates. These may be quickly and accurately obtained with the aid of a computer programme.

The use of the interference equations in the blade design procedure, results in aspect ratio 1 blade angles to differ by a maximum of two degrees from those for aspect ratio 2. Depending on the manufacture accuracy, a difference of this order may either be enlarged or reduced, and since such an accuracy was considered questionable, blade design values were the same for both aspect ratios. Blade surface co-ordinates values for the low aspect ratio were twice those for the higher aspect ratio.

A.2 Design geometry and other data

All the blades have simple cylindrical root platforms and threaded root fixings. When any one set of blades is built in the compressor*, the axial spacing between any two neighbouring rows of blades was kept at a minimum of 0.500 inches, to allow access of instrumentation in the space between the blade rows and to any radial location without risking damage to the instrument. Blade tip clearance was kept at 0.060 inches.

The pertinent design details for both blade designs are listed in Table I.

APPENDIX B /

---

* Plates 3 and 4 show a representative set-up of the exponential blades.

APPENDIX B

Flow Calculations* with Losses

"Loss" calculations were made using actuator disc theory, employing the same equations used for the inviscid calculations of Ref.6. The only difference was that in the "loss" calculations both total pressure losses (two dimensional, secondary and clearance) and angle variation due to secondary flow were introduced.

B.1 Total pressure losses

By employing all the assumptions and restrictions outlined in Ref.6, the differential equation with total pressure loss is obtained from the Bragg-Hawthorne expression for non-isentropic flow,

$$\frac{dH}{d\psi} - T\frac{dS}{d\psi} = \frac{1}{r^2}\left(\eta \cdot r + \theta\frac{d\theta}{d\psi} \right) \qquad \ldots(B.1)$$

Following on in the same fashion as in Ref.6, eqn. (B.1) may be linearised by writing $d\psi = c_{x,i} r dr$, from which a differential equation for $c_{x,i}$ may be obtained, thus,

$$c_{x,i}\frac{dc_{x,i}}{dr} + \frac{c_{\theta,ie}}{r}\frac{d(rc_{\theta,ie})}{dr} = \frac{dH_{ie}}{dr} - T\frac{dS_{ie}}{dr} \qquad \ldots(B.2)$$

where $i = 1, 2, 3\ldots$

Horlock[13] shows that for the adiabatic, incompressible flow across a stationary row of blades

$$T\frac{dS}{dr} = \frac{1}{\rho} \cdot \frac{d\Delta P}{dr} \qquad \ldots(B.3)$$

where ΔP is the total pressure loss measured relative to a stationary row.

Substitution of eqn. (B.3) into (B.2) gives

$$c_{x,i}\frac{dc_{x,i}}{dr} + \frac{c_{\theta,ie}}{r} \cdot \frac{d(rc_{\theta,ie})}{dr} = \frac{dH_{ie}}{dr} - \frac{1}{\rho} \cdot \frac{d\Delta P}{dr} \qquad \ldots(B.4)$$

Similarly/

---

* Further details of these calculations are given in Ref.5.

Similarly for a rotating blade row, with

$$T\frac{ds}{dr} = \frac{1}{\rho} , \frac{d\Delta P'}{dr} \qquad \text{...(B.5)}$$

where $\Delta P'$ is the total pressure loss measured relative to a moving row.

B.1.1 Skin friction losses on blade surfaces

The effect of skin friction on the blade surface is to cause irreversibilities in the flow, leading to an increase in entropy and loss in total pressure across the blade row.

The total pressure loss arising from skin friction on the blade surfaces may be based on Lieblein's low-speed relationship between the equivalent diffusion (D_{eq}) and the wake momentum-thickness parameter (W_{mt}), at any flow condition. This relationship, for a compressor with parallel wall annulus is

$$D_{eq} = \left[K_1 + K_2(i - i^*)^{K_3} + K_4 \,.\, \frac{s.\cos^2\beta_{in}}{C} \,.\, \left(\tan\beta_{in} - \frac{c_{x,out}}{c_{x,in}} \,.\, \tan\beta_{out} \right) \right] \times$$

$$\times \frac{\cos\beta_{out}}{\cos\beta_{in}} \,.\, \frac{c_{x,in}}{c_{x,out}} \qquad \text{...(B.6)}$$

and can be applied to rotors and stators. K_1 , K_2 , K_3 and K_4 are constants.

Using Swan's statistical curve fit for rotors, Fig.7, a value for the wake-momentum thickness $W_{mt,rt}$ may be obtained. Similarly, using Lieblein's experimental curve, given as independent of radial location, Fig.7, for the variation of D_{eq} with W_{mt} for C4 circular-arc blades at and off minimum loss conditions, a value for $W_{mt,st}$ may be obtained.

The approximate expression for W_{mt} then gives the required total pressure loss coefficient, thus,

$$\sigma_{cf} = \frac{2C,\, W_{mt}}{s.\cos\beta_{out}} \left(\frac{\cos\beta_{in}}{\cos\beta_{out}} \right)^2 \qquad \text{...(B.7)}$$

where

$$\sigma_{cf} = \frac{(\Delta P_{cf})_{st}}{\frac{1}{2}\rho c^2{}_{in}} \quad \text{for a stator} \qquad \text{...(B.8)}$$

$$\sigma_{cf} = \frac{(\Delta P'{}_{cf})_{rt}}{\frac{1}{2}\rho w^2{}_{in}} \quad \text{for a rotor} \qquad \text{...(B.9)}$$

The/

The inlet guide vanes skin friction loss is based on Ainley's nozzle blades minimum profile loss[14] and its total pressure loss coefficient is defined as

$$\sigma_{cf} = \frac{(\Delta P_{cf})_{igv}}{\frac{1}{2}\rho c^2_{out}} \qquad \ldots(B.10)$$

B.1.2 Tip clearance flow losses

The total pressure loss arising from tip clearance flow is obtained from a formula given by Vavra[15] for the tip clearance drag coefficient. Vavra, using a flow model devised by Rains, derived the following formula:

$$C_{Dt} = 0.29 \, . \, C_L^{\frac{3}{2}} \, . \, \frac{tc}{L} \qquad \ldots(B.11)$$

where tc is the tip clearance.

The drag coefficient for a compressor cascade is related to the total pressure loss coefficient; thus,

$$C_D = \frac{\Sigma \, . \, s}{C} \, . \, \frac{\cos^3 \bar{\alpha}}{\cos^2 \alpha_{in}} \qquad \ldots(B.12)$$

and for an igv or turbine cascade thus,

$$C_D = \frac{\Sigma \, . \, s}{C} \, . \, \frac{\cos^3 \bar{\alpha}}{\cos^2 \alpha_{out}} \qquad \ldots(B.13)$$

where $\bar{\alpha} = \arctan \left(\frac{\tan \alpha_{in} + \tan \alpha_{out}}{2} \right)$.

By combining eqns. (B.11) and (B.12) we have for a compressor cascade

$$\Sigma_t = 0.29 \, . \, C_L^{\frac{3}{2}} \, . \, \frac{tc}{L} \, . \, \frac{C}{s} \, . \, \frac{\cos^2 \alpha_{in}}{\cos^3 \bar{\alpha}} \qquad \ldots(B.14)$$

and by combining eqns. (B.11) and (B.13), we have for a compressor cascade

$$\Sigma_t = 0.29 \, . \, C_L^{\frac{3}{2}} \, . \, \frac{tc}{L} \, . \, \frac{C}{s} \, . \, \frac{\cos^2 \alpha_{out}}{\cos^3 \bar{\alpha}} \qquad \ldots(B.15)$$

B.1.3/

B.1.3 Cascade secondary flow losses

Vavra's empirical relation for the induced drag coefficient due to secondary flow is used. This relation is

$$C_{Dcs} = 0.04 \cdot \frac{C_L^2}{AR} \qquad \ldots(B.16)$$

By combining eqns. (B.12) and B.16), we have for a compressor cascade,

$$\Sigma_{cs} = 0.04 \cdot \frac{C_L^2}{AR} \cdot \frac{C}{s} \cdot \frac{\cos^2\alpha_{in}}{\cos^3\overline{\alpha}} \qquad \ldots(B.17)$$

Similarly, for a turbine cascade,

$$\Sigma_{cs} = 0.04 \cdot \frac{C_L^2}{AR} \cdot \frac{C}{s} \cdot \frac{\cos^2\alpha_{out}}{\cos^3\overline{\alpha}} \qquad \ldots(B.18)$$

The drag coefficients C_{Dt} and C_{Dcs} given by eqns. (B.11) and (B.16) respectively are energy averaged over the whole blade length. The derived pressure loss coefficients Σ_t and Σ_{cs} will also be averaged in the same way. In order that these coefficients may be used for a particular blade element, new coefficients σ_t, σ_{cs}, referred to these elements, must be calculated, where σ_t and σ_{cs} are each defined in a similar way as σ_{cf} in eqns. (B.8), (B.9) and (B.10). Such a calculation is detailed in Ref.5; essentially the loss is assumed to vary parabolically from zero at the edge of the boundary layer to a maximum at the wall. The integral of this local loss is equal to the "Vavra" overall loss. The thickness of the boundary layer is assumed to remain constant through the compressor at the entry value.

B.1.4 Equations with total pressure loss

The equation with total pressure loss is obtained by substituting eqns. (A.4) and (A.5) into eqn. (B.4), it being assumed that an overall total pressure loss coefficient may be defined for the region outside the boundary layer as

$$\sigma = \sigma_{cf} \qquad \ldots(B.19)$$

and for the region within the boundary layer* as

$$\sigma = \sigma_{cf} + \sigma_t + \sigma_{cs} \qquad \ldots(B.20)$$

For the case of the single-stage compressor, eqn. (B.4) in its new form may be applied across each blade row. Three simultaneous differential equations (including total pressure loss) for the "infinity" distributions of axial velocity, are thus obtained.

In/

---

* In the region where there is no tip clearance, $\sigma_t = 0$.

In non-dimensional form these equations become:

$$\begin{aligned} b_{11} V_1 + b_{12} V_2 + b_{13} V_3 + E_1 &= 0 \\ b_{21} V_1 + b_{22} V_2 + b_{23} V_3 + E_2 &= 0 \\ b_{31} V_1 + b_{32} V_2 + b_{33} V_3 + E_3 &= 0 \end{aligned} \qquad \ldots(B.21)$$

where

$$V_1 = \frac{d}{dR}\left[\frac{c_{x,1}}{c_{x,o}}\right], \quad V_2 = \frac{d}{dR}\left[\frac{c_{x,2}}{c_{x,o}}\right], \quad V_3 = \frac{d}{dR}\left[\frac{c_{x,3}}{c_{x,o}}\right]$$

and b_{jk}, E_j may be functions of R, $c_{x,j}$, tan (α_e or β_e),

$$\frac{d}{dR}\left[\tan(\alpha_e \text{ or } \beta_e)\right], \ \phi, \ AR, \ \sigma \text{ and } \frac{d\sigma}{dR}$$

A complete statement of eqn. (B.21) is given in Ref.5, Fig.8, shows a distribution of the calculated total pressure loss coefficients with radius for the i.g.v., rotor and stator blade rows.

B.2 Outlet angle variation due to secondary flows

The tracing of the secondary vorticities through a single-stage compressor is detailed in Refs.5 and 16. With the streamwise vorticity components at exit from each row determined, the induced secondary velocities and the associated changes in outlet air angles is then calculated from Hawthorne's series solution. For this solution, Hawthorne[17] has shown that series terms with n > 1 are small and therefore may be neglected.

If the streamwise vorticity at exit from a two-dimensional cascade of the same geometry as the tip section is $\xi_s(z)$, where z is the distance from the wall, then the mean change of outlet angle across the blade pitch at a point Z from the wall is given for $o < Z < \delta$ by

$$\tan\left(\Delta\alpha_{out}(Z)\right) = \frac{8}{\pi^2 c_{x,e}} \cdot \left[\frac{\cos h \frac{\pi Z}{\gamma}}{\sin h \frac{\pi L}{\gamma}} \int_Z^{\delta} \xi_s(z) \sin h \frac{\pi}{\gamma}(L - z)\,dz - \frac{\cos h \frac{\pi}{\gamma}(L - Z)}{\sin h \frac{\pi L}{\gamma}} \int_o^{Z} \xi_s(z) \sin h \frac{\pi z}{\gamma}\,dz\right] \qquad \ldots(B.22)$$

and/

and for $Z > \delta$ by

$$\tan\left(\Delta\alpha_{out}(Z) \right) = \frac{8}{\pi^2 c_{x,e}} \cdot \frac{\cos h \frac{\pi}{y}(L - Z)}{\sin h \frac{\pi L}{y}} \int_{0}^{\delta} \xi_s(z) \sin h \frac{\pi z}{y}\, dz \qquad \ldots(B.23)$$

where $y = s \cdot \cos \alpha_{out}$.

If the radial distribution of outlet angle based on two-dimensional cascade data is $\alpha_{out}(r)$, then the distribution corrected for the secondary flow is given by

$$\alpha_{out(c)}(r) = \alpha_{out}(r) + \Delta\alpha_{out}(r) \qquad \ldots(B.24)$$

where $\Delta\alpha_{out}(r_t - r)$ is assumed to be the same as $\Delta\alpha_{out}(Z)$, the two-dimensional calculation.

B.3 Calculation procedure

For the single-stage compressor, eqns. (B.21) are to be solved simultaneously. The method of solution is outlined in Ref.6.

To solve eqns. (B.21), an estimate of the radial distribution of the total pressure loss coefficients and the outlet air angles for each blade row is required. Such an estimate is obtained as follows:

(a) Obtain the "infinity" and "trailing edge" distributions of axial velocity from a solution to eqns. (B.21) with the total pressure loss coefficients made equal to zero and the outlet air angles taken to be those at design (the three-dimensional, inviscid solution, Ref.6).

(b) Assume a velocity profile at entry to the compressor stage consisting of n^{th} power law distribution in the inner and outer wall boundary layer and a uniform distribution outside it, Ref.6.

(c) Calculate the entry vorticity and then trace the secondary vorticities through the compressor stage using the design outlet air angles, Ref.16.

(d) For each blade row

   (i) Calculate the change in the air outlet angle $\Delta\alpha_{out}(r)$ from eqns. (B.22) and (B.23) using $c_{x,e}(r)$ obtained in (a) and $\xi_s(r)$ obtained in (c).

   (ii) Obtain the new distribution of air outlet angle $\alpha_{out(c)}(r)$ corrected for the secondary flow from (B.24).

   (iii) Calculate $\sigma(r)$ using $c_{x,e}(r)$ obtained in (a) and the design outlet air angles.

(e) /

(e) Re-solve eqns. (B.21) with estimates for $\sigma(r)$ from d(iii) and for $\alpha_{out(c)}(r)$ from d(ii)* to obtain a new distribution of "infinity" and "trailing edge" axial velocity.

(f) Re-trace the secondary vorticity using the same entry velocity profile assumed in (b) and $\alpha_{out(c)}(r)$ obtained in d(ii).

(g) Re-calculate $\Delta\alpha_{out}(r)$ and $\sigma(r)$ for each blade row using $c_{x,e}(r)$ obtained in (e), $\xi_s(r)$ obtained in (f) and $\Delta\alpha_{out(c)}(r)$ obtained in d(ii), and use these as new estimates in the next approximation.

(h) Repeat steps (e), (f) and (g), until no further change in the $c_{x,e}$ distribution for each row is obtained.

APPENDIX C/

---

* Horlock[16] has shown that the use in an actuator disc analysis of the exit air angle as calculated from eqns. (B.22) and (B.23) is justified, the streamwise vorticity being approximately the same at exit from the row of widely spaced blades and the equivalent actuator disc.

APPENDIX C

NOTATION

c_r, c_θ, c_x	Velocity components in r, θ, x co-ordinates system
R	Dimensionless radius ($= r/r_t$)
α	Absolute flow angle at entry or exit from a stator row measured from the x-direction
β	Relative flow angle at entry or exit from a rotor row measured from the x-direction
Ω	Angular velocity
U	Blade speed ($= \Omega r$)
c, w	Absolute, relative velocity
C	Chord length
X	Distance from actuator disc (always positive)
L	Blade length ($= r_t - r_h$)
h, H	Static, total enthalpy
p, P	Static, total pressure
ΔP, $\Delta P'$	Absolute, relative total pressure loss
Σ	Total pressure loss coefficient integrated over the blade length
σ	Total pressure loss coefficient referred to a blade element
C_D	Two-dimensional drag coefficient
$R\hat{e}$	Reynolds number $\left(= \dfrac{U_m \cdot C}{\nu}\right)$
S	Entropy
s	Blade spacing
γ	$s.\cos(\alpha_e \text{ or } \beta_e)$
ϕ	Flow coefficient ($= c_{x,o}/U_m$)
AR	Aspect ratio ($= L/C$)
K	Constant ($= r_t/r_m$)
λ	$c_{x,e}/c_{x,o}$

V	$d\lambda/dR$
f	$\tan(\alpha_e \text{ or } \beta_e)$
F	df/dR
X	$d\sigma/dR$
ρ	Mean air density
η	Vorticity component in θ-direction
Y, Z	Co-ordinate system at exit from two-dimensional cascade (Y perpendicular to streamline, Z along blade).
z	A parameter replacing Z
δ	Boundary layer thickness
tc	Tip clearance
ξ, ζ	Absolute, relative vorticity
ψ	Stream function
θ	$r.c_\theta$
B	Barometric pressure
T	Ambient temperature (absolute)
Δp	Static pressure rise
ε	Flow angle of turning through a blade row
i	Flow angle of incidence onto a blade row
W_{mt}	Wake momentum thickness
D_{eq}	Equivalent diffusion factor
$\Delta\alpha_e$	Change in flow outlet angle due to secondary flow
Δp_d	Manometer static pressure depression

<u>Subscripts</u>

o	Entry conditions
1, 2, 3	Radial equilibrium conditions (that would be attained far downstream of a blade row)
1e, 2e, 3e	Positions of the trailing edges of blade rows
s, n	Parallel and normal to streamline

igv, rt, st/

igv, rt, st	Pertaining to inlet guide vane, rotor and stator respectively
sf	Due to skin friction
tc	Due to tip clearance
cs	Due to cascade secondary flow
t, m, h	Tip, mean and hub respectively
in, out	At inlet to and outlet from a blade row
max	Maximum
I	Indicated
T	True
g	Gauge (i.e., relative to atmospheric pressure)

Superscripts

-	Mean Value
'	Relative to a row

REFERENCES/

Footnote: Wherever two or more subscripts are used together, a comma has been used to separate them; e.g., $c_{x_{o_{max}}}$ is written $c_{x,o,max}$.

REFERENCES

No.	Author(s)	Title, etc.
1	J. H. Horlock R. Shaw D. Pollard A. K. Lewkowicz	Reynolds number effects in cascades and axial-flow compressors. Trans. A.S.M.E., Series A, 86, 236. (1964)
2	D. Pollard	The low speed performance of two-dimensional cascades of aerofoil. Ph. D. Thesis, Liverpool University. (1964)
3	M. R. A. Shaalan	The stalling performance of cascades of different aspect ratios. Ph. D. Thesis, Liverpool University. (1967)
4	J. A. Fligg, Jr.	Tests of a low-speed three-stage axial flow compressor at aspect ratios of one, two and four. AIAA Paper No. 66-613. (1966)
✓ 5	G. J. Fahmi	The effect of blade aspect ratio on the performance of axial flow compressors. Ph. D. Thesis, Liverpool University. (1967)
6	J. H. Horlock G. J. Fahmi	A theoretical investigation of the effect of aspect ratio on axial-flow compressor performance. ARC C.P. No.943. (1966)
7	R. Shaw A. K. Lewkowicz	The construction and testing of a large axial-flow compressor. ARC C.P. No.620. (1962)
8	J. H. Horlock	Instrumentation used in measurement of the three-dimensional flow in an axial-flow compressor. ARC C.P. No.321. (1955)
9	J. H. Horlock E. C. Deverson	An experiment to determine the position of an equivalent actuator disc replacing a blade row of a turbomachine. ARC.C.P. No.426. (1958)
10	J. H. Horlock	Communication relating to the paper "Three-dimensional design of multi-stage axial flow compressors" by J. W. Railly. J. Mech. Eng. Sci. 3, No. 3, 286. (1961)
✓ 11	A. D. Carmichael J. H. Horlock	Actuator disc theories applied to the design of axial-flow compressors. ARC C.P. No.315 (1956)
12	A. R. Howell	The present basis of axial-flow compressor design. ARC R.& M.2095. (1942)
13	J. H. Horlock	Axial-flow compressors - fluid mechanics and thermodynamics. Butterworths, London. (1958)

No.	Author(s)	Title, etc.
✓ 14	J. H. Horlock	Losses and efficiences in axial-flow turbines. Int. J. Mech. Sci. 2., 1, 48-75. (1960)
✓ 15	M. H. Vavra	Aero-thermodynamics of fluid flow in turbomachinery. John Wiley, New York. (1960)
16	J. H. Horlock	Annulus wall boundary layers in axial compressor stages. J. Basic Eng., 85, D, 1, 55-61. (1963)
17	W. R. Hawthorne	Some formulae for the calculation of secondary flow in cascades. A.R.C.17 519. (1955)

BW

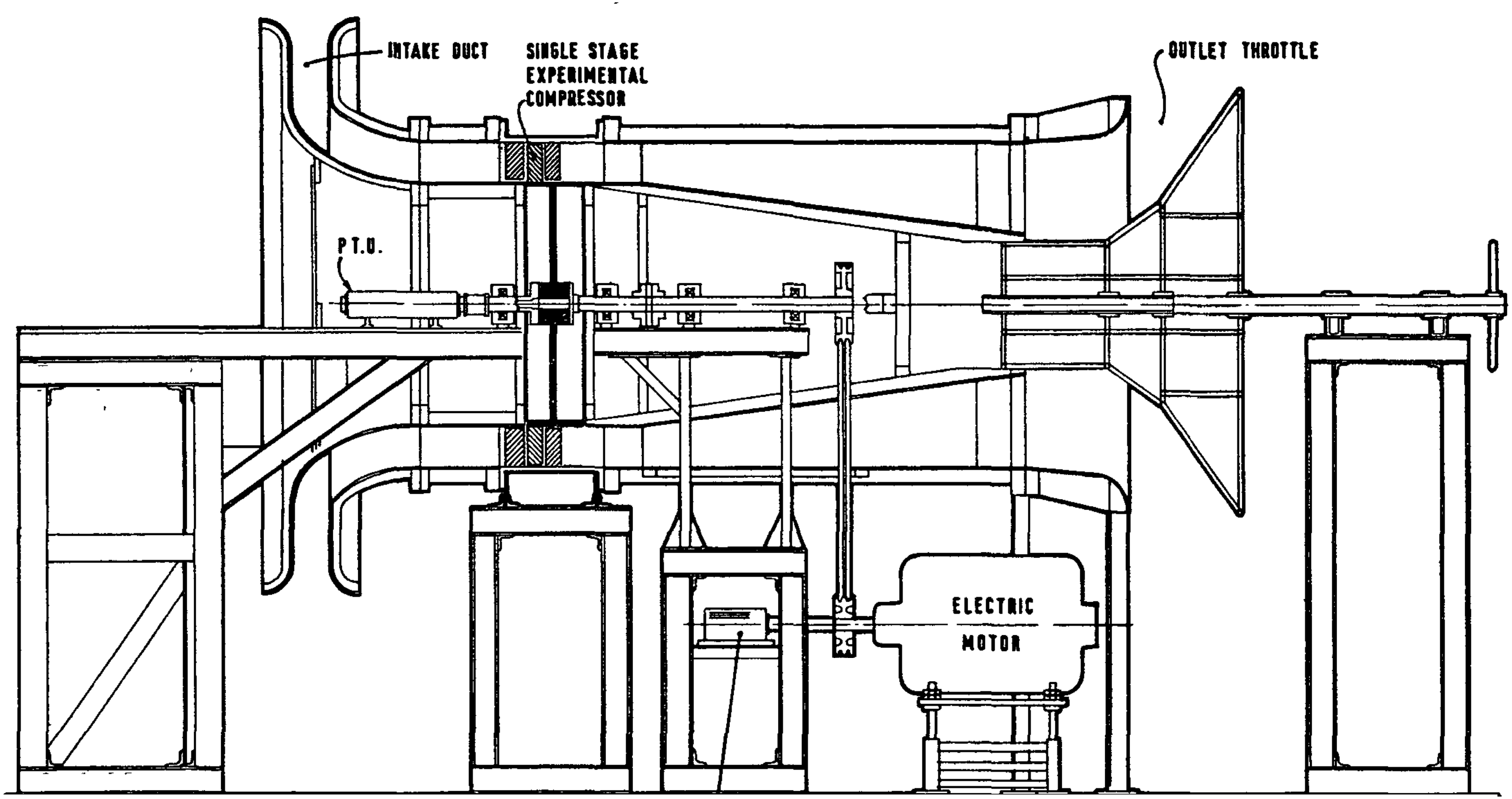

FIG 1. DIAGRAMATIC LAYOUT OF RIG

PLANE Nº	ANNULUS AREA in²	INSTRUMENTATION
P 1	1336 5	5 - STATIC TAPPINGS, EQUALLY SPACED ON EACH OF FRONT AND REAR WALLS, PROVISION FOR TRAVERSING
P 2	791 8	5 - STATIC TAPPINGS, EQUALLY SPACED ON EACH OF INNER AND OUTER WALLS, PROVISION FOR RADIAL TRAVERSING
P 3	″	12 - STATIC TAPPINGS IN OUTER WALL, OVER ONE BLADE PITCH - PROVISION FOR RADIAL AND CIRCUMFERENTIAL TRAVERSING
P 4	″	AS P2 - BUT 2 INNER WALL STATIC TAPPINGS - PROVISION FOR CIRCUMFERENTIAL TRAVERSING
P 5	″	AS P4 — 1 INNER WALL STATIC TAPPING ON ROTOR DRUM
P 6	″	AS P5
P.7	″	AS P.3
P.8	″	AS P3 - ALSO 3 INNER WALL STATIC TAPPINGS
P.9	″	AS P2 - NO PROVISION FOR TRAVERSING

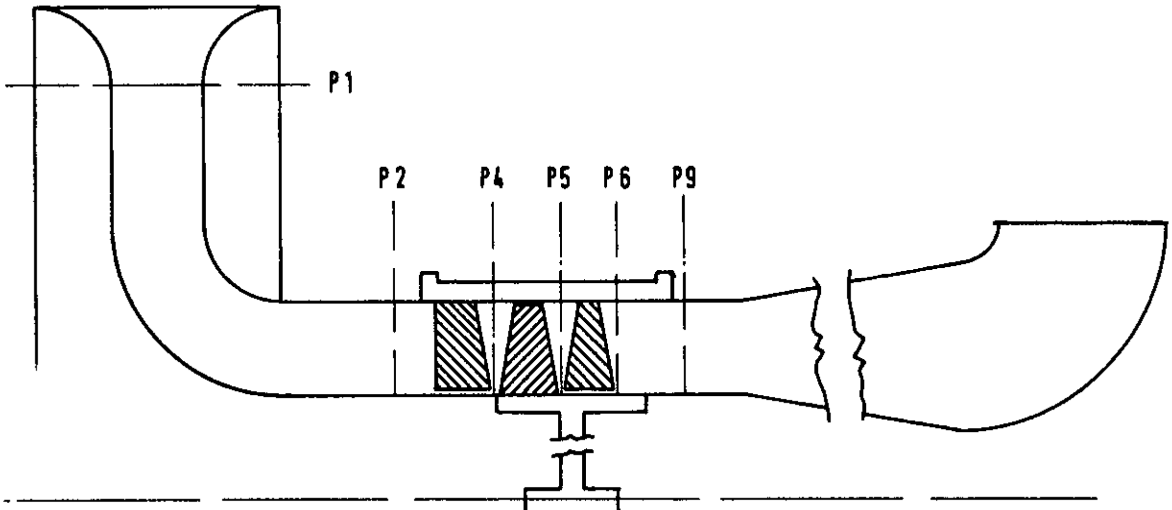

2a Short Chord Blades A.R = 2

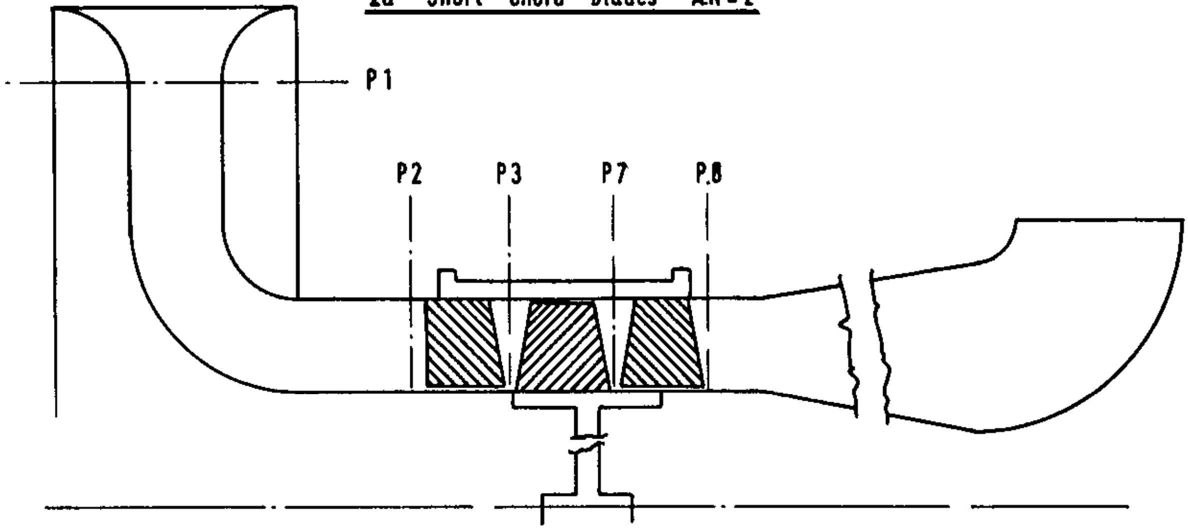

2b. Long Chord Blades A.R = 1

FIG 2a.b. INSTRUMENT TRAVERSE and STATIC TAPPING PLANES

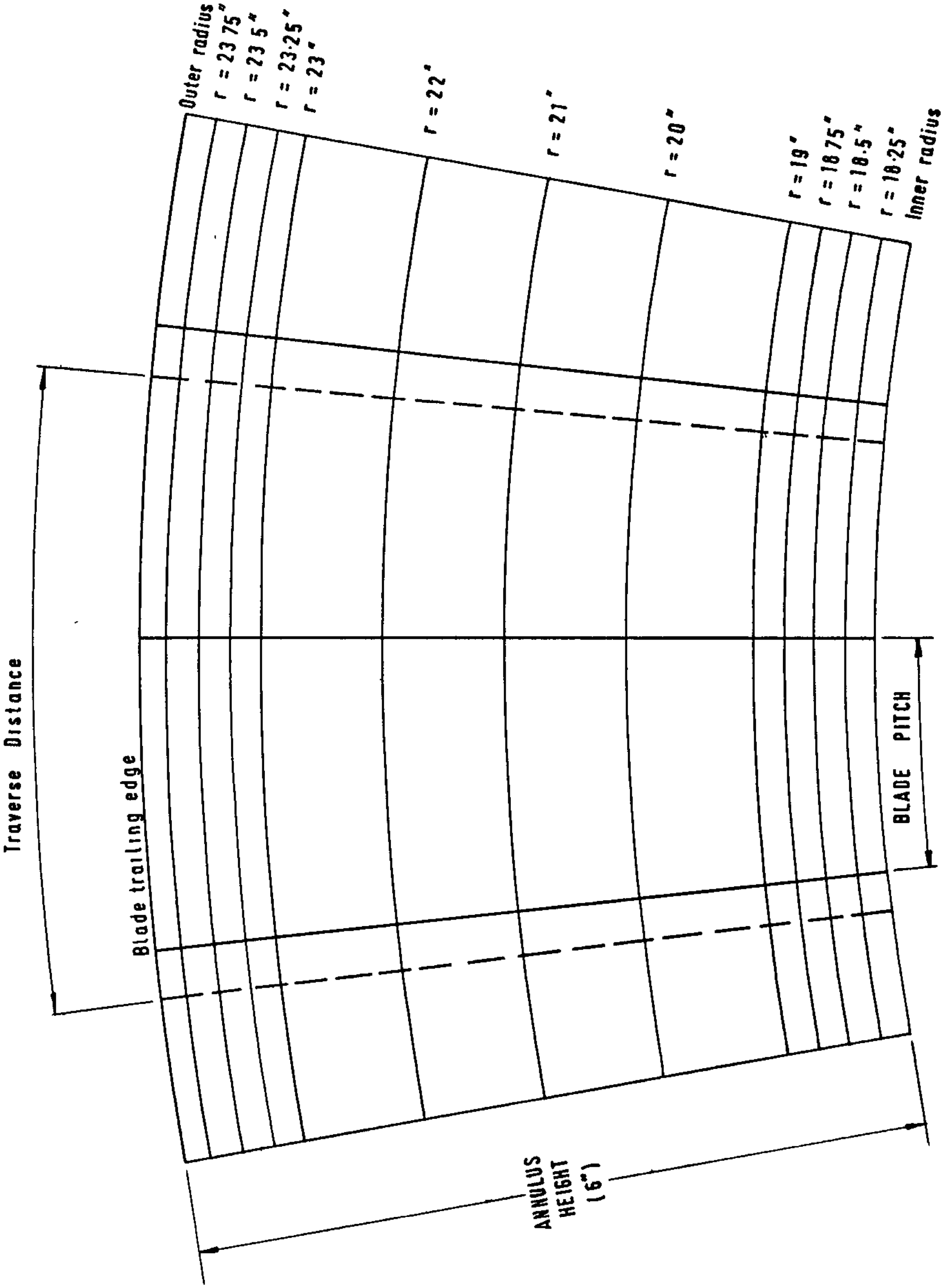

FIG. 3. CIRCUMFERENTIAL PLANES OF TRAVERSE

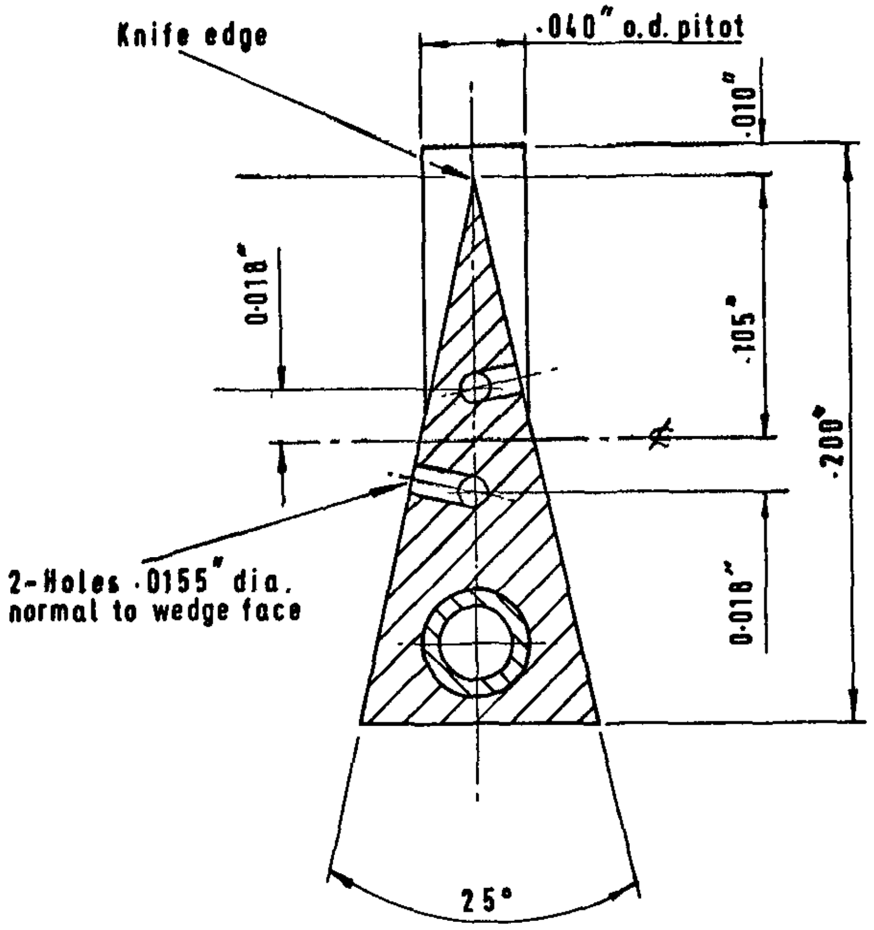

ENLARGED SECTION A-A

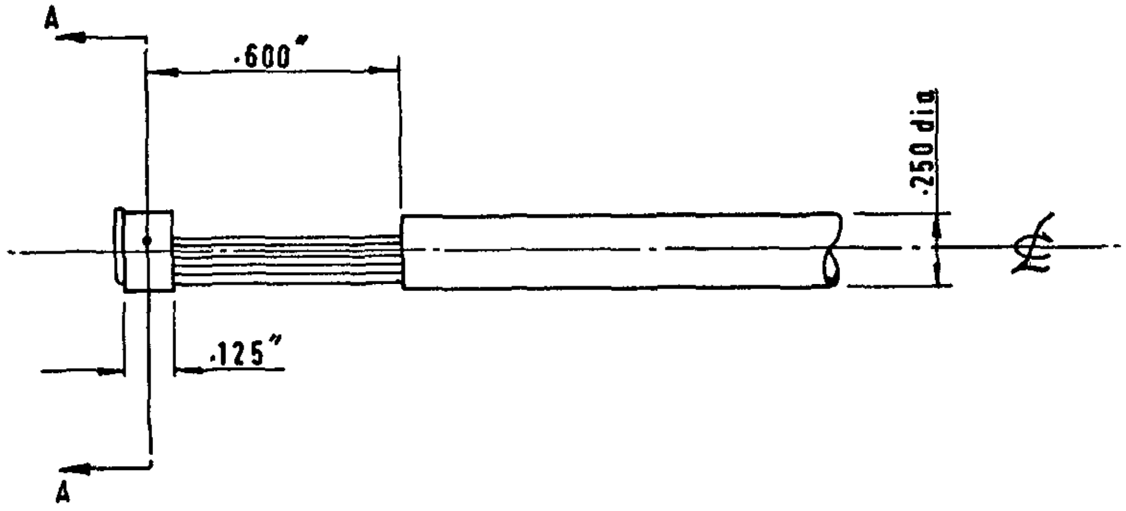

FIG.4. WEDGE PROBE DETAIL

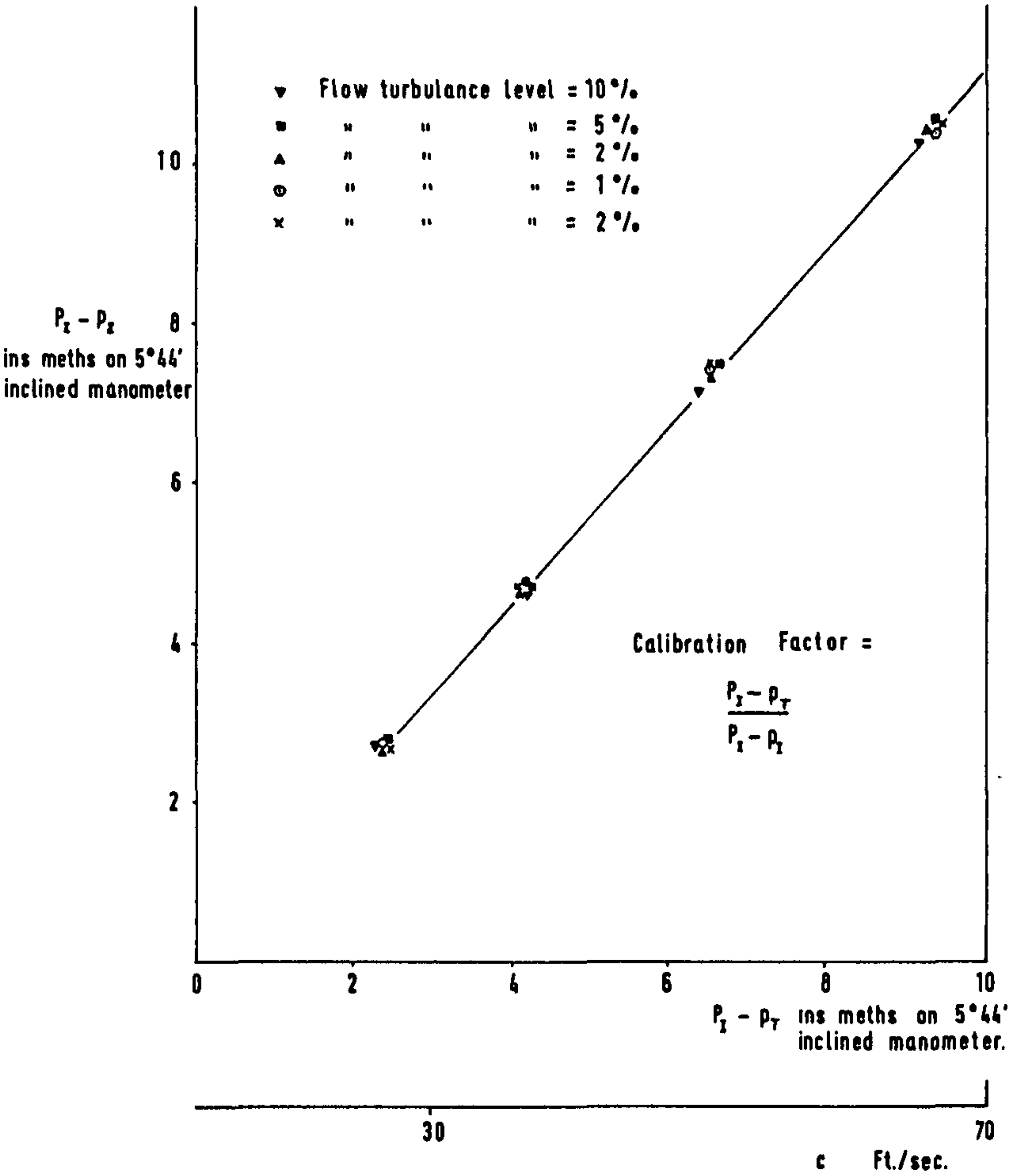

FIG. 5. WEDGE INSTRUMENT CALIBRATION CURVE

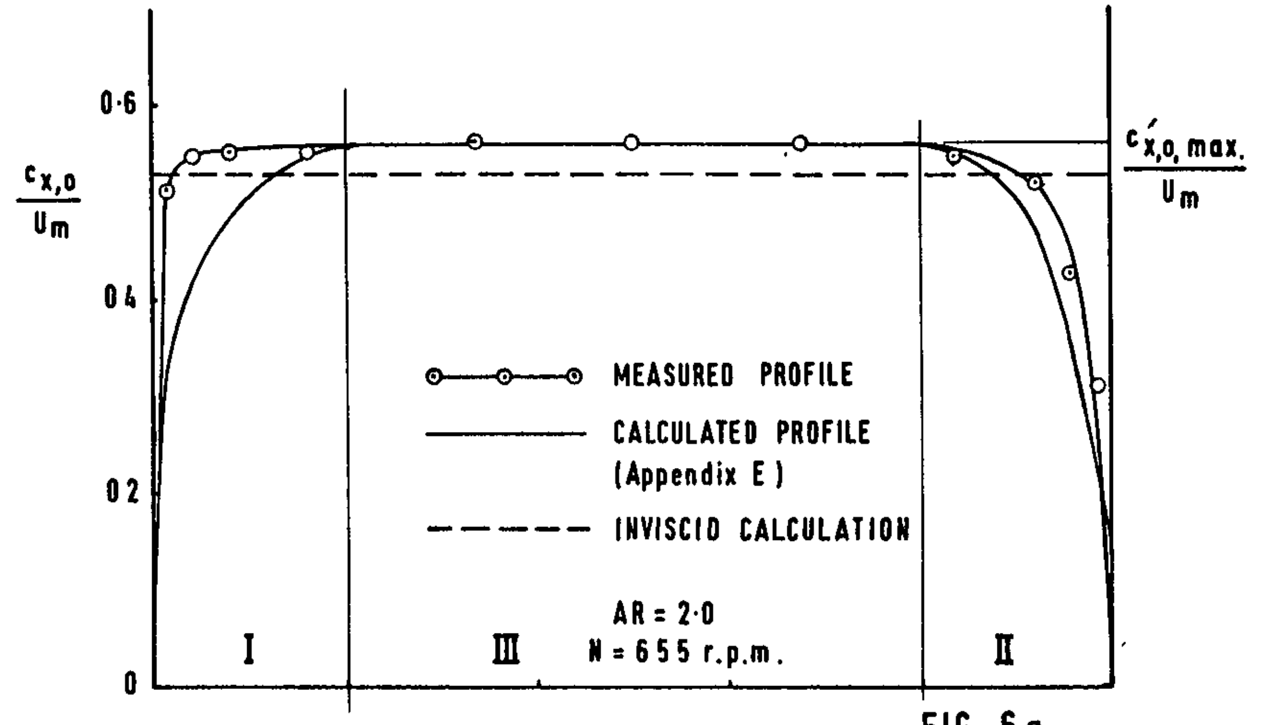

FIG. 6a

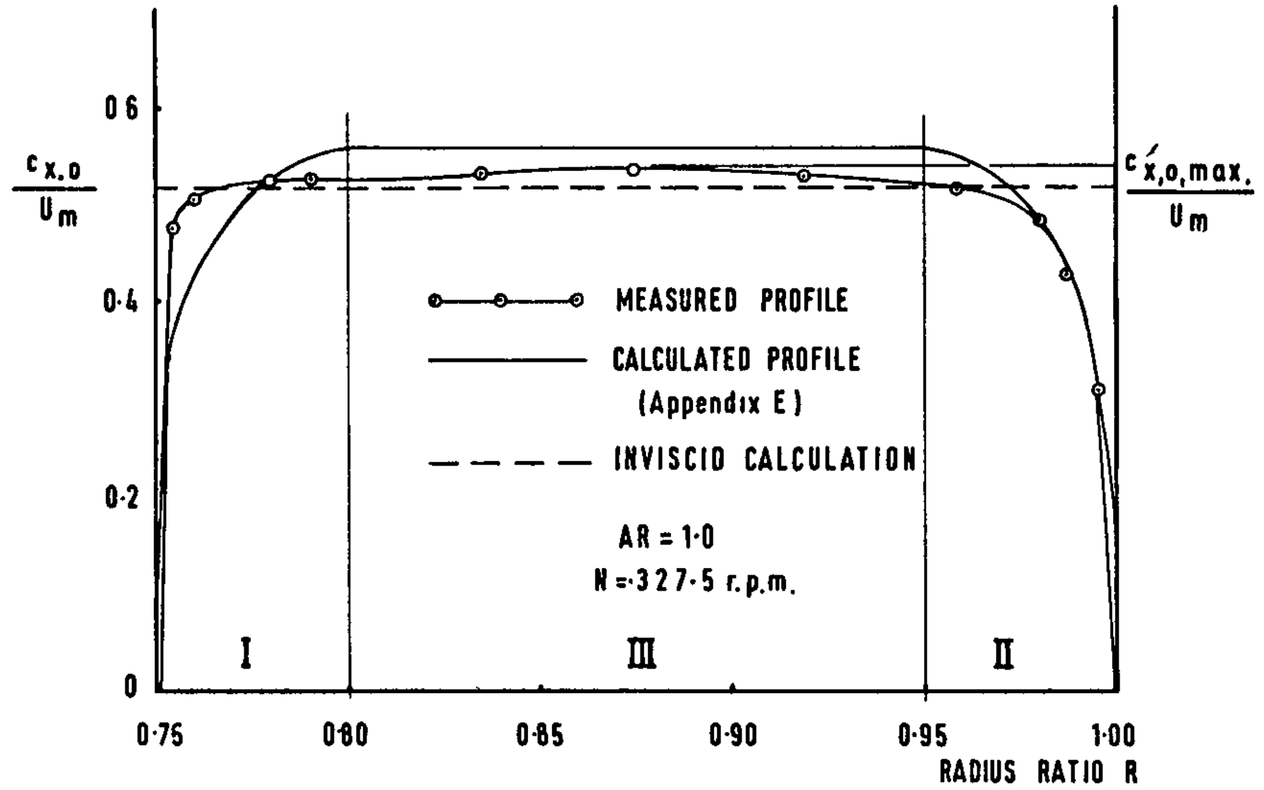

FIG. 6 b

FIG. 6 a,b THE ENTRY VELOCITY PROFILE

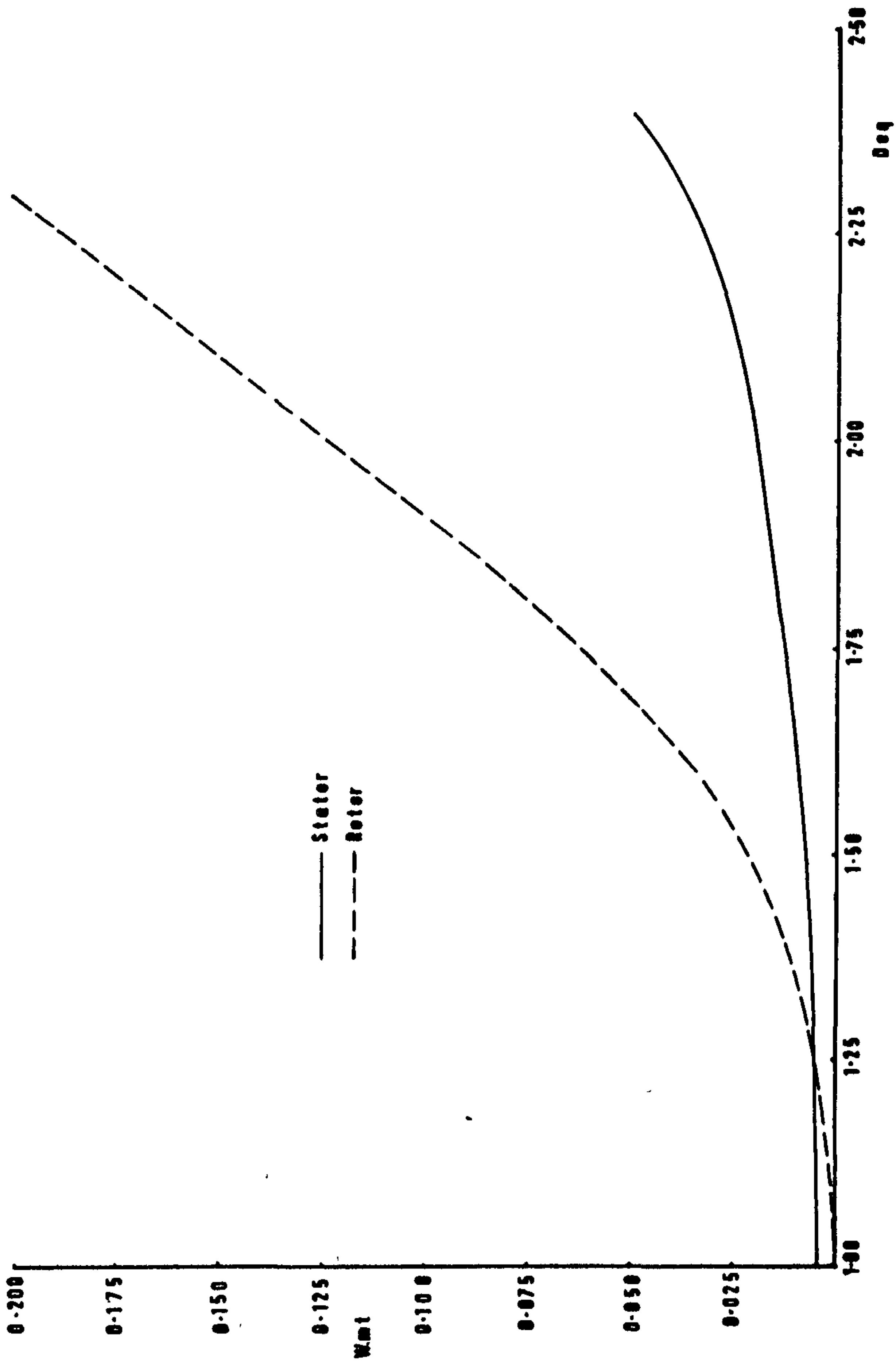

FIG. 7 ROTOR AND STATOR LOSS ESTIMATION CURVES

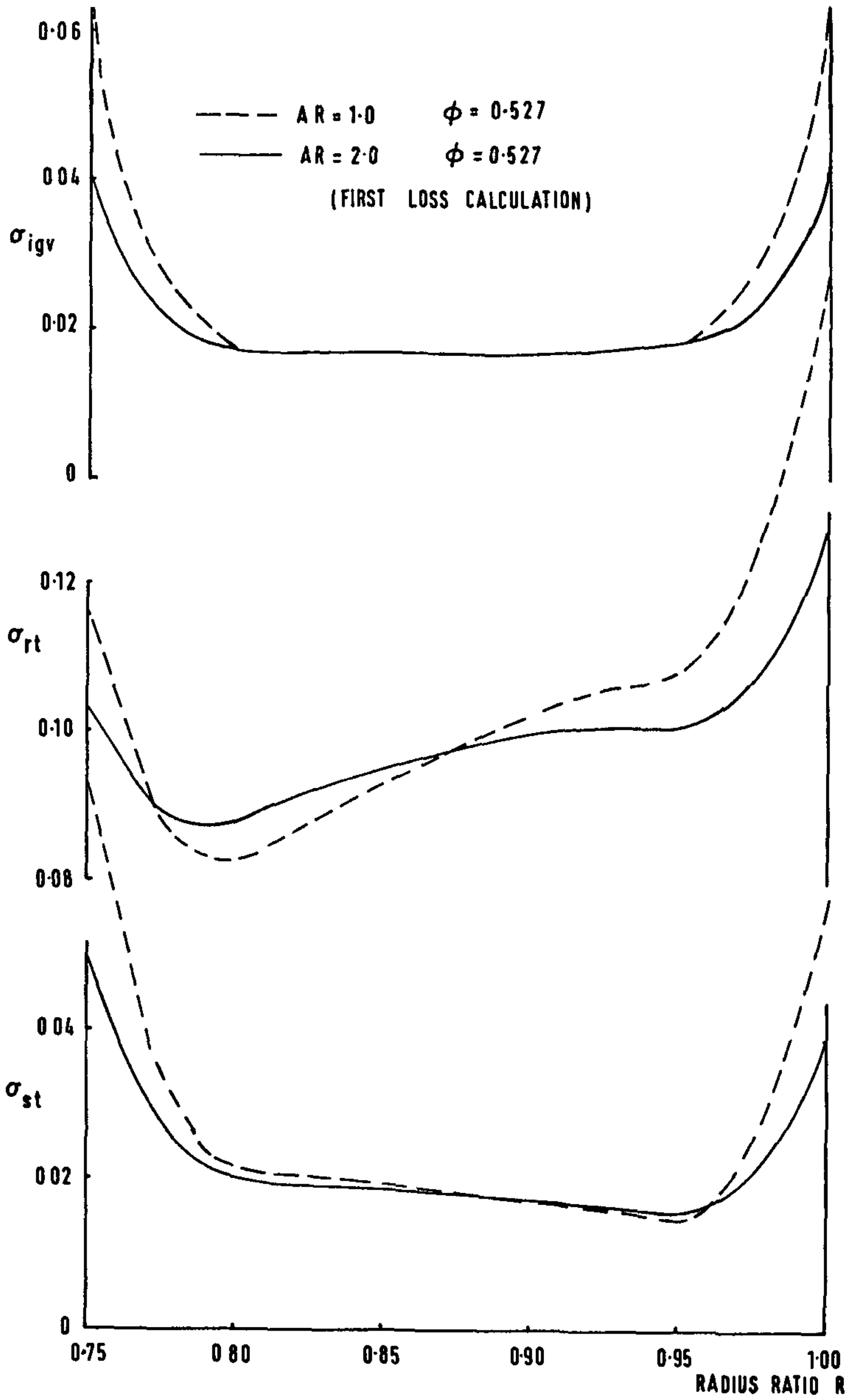

FIG. 8 RADIAL DISTRIBUTION OF OVERALL TOTAL PRESSURE LOSS COEFFICIENT

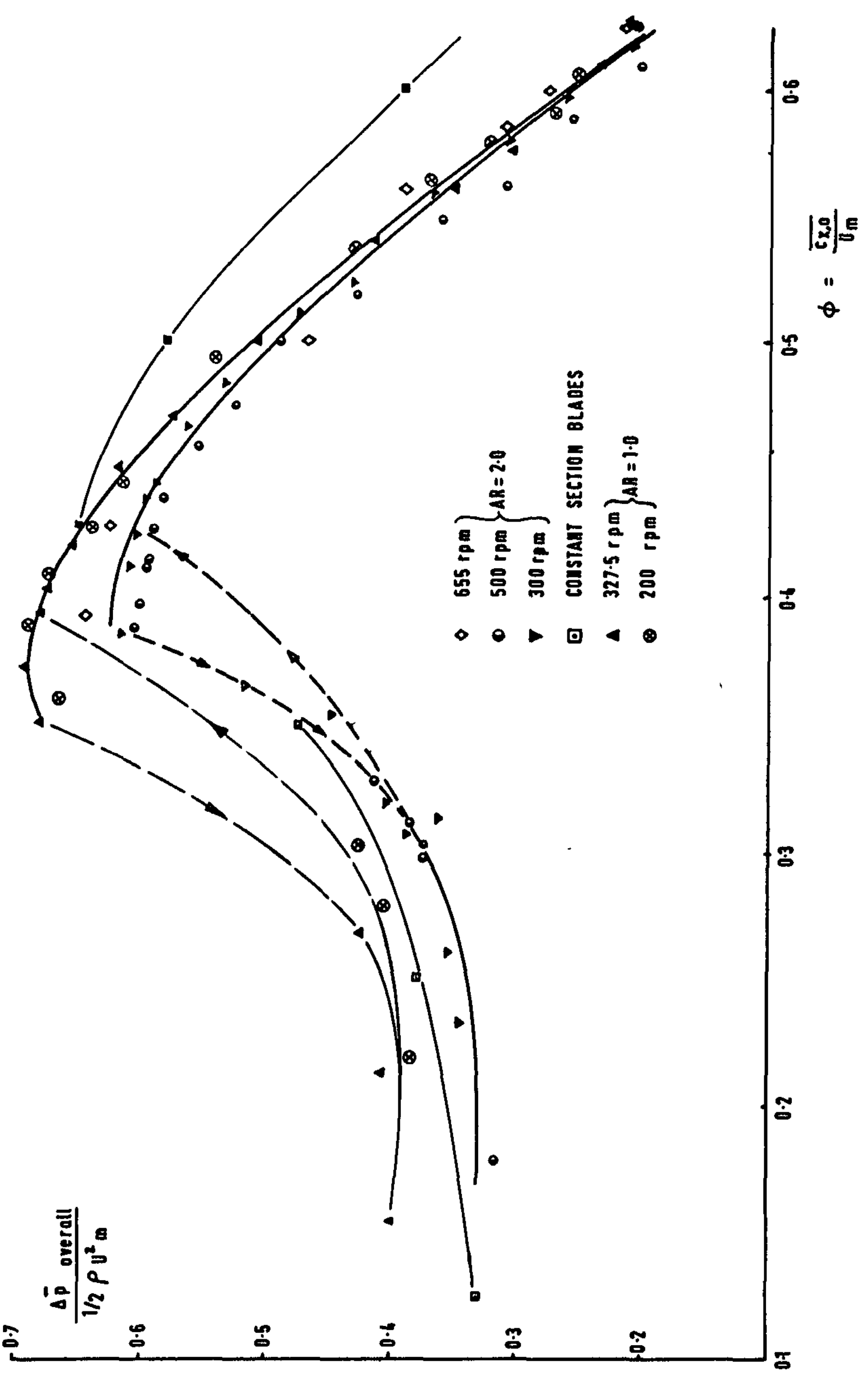

FIG. 9 OVERALL CHARACTERISTICS OF THE VARIOUS COMPRESSOR BUILDS

FIG. 10 CONDITIONS AT ENTRY TO COMPRESSOR STAGE (A.R. = 2)

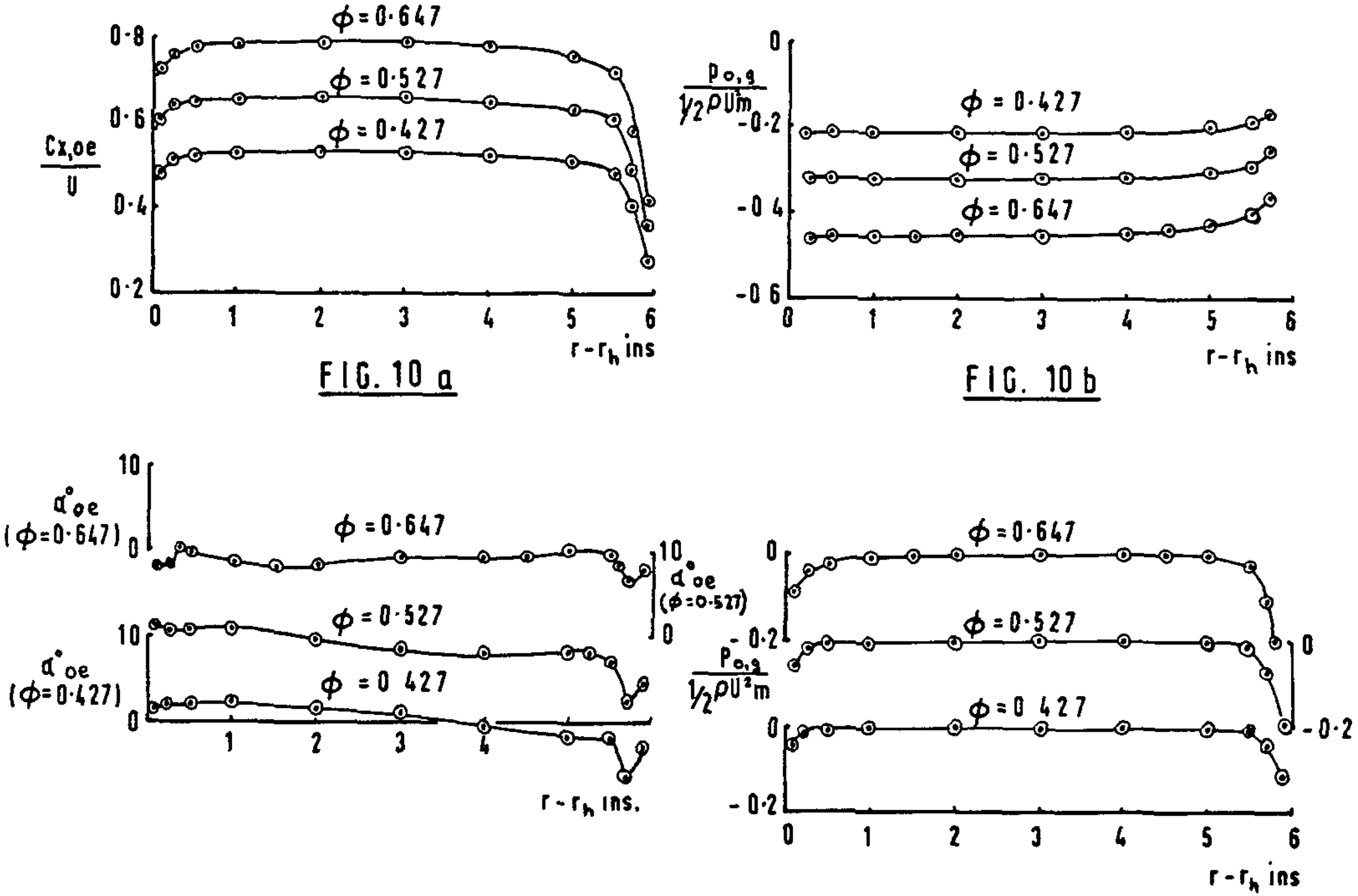

FIG. 10c

FIG. 10d

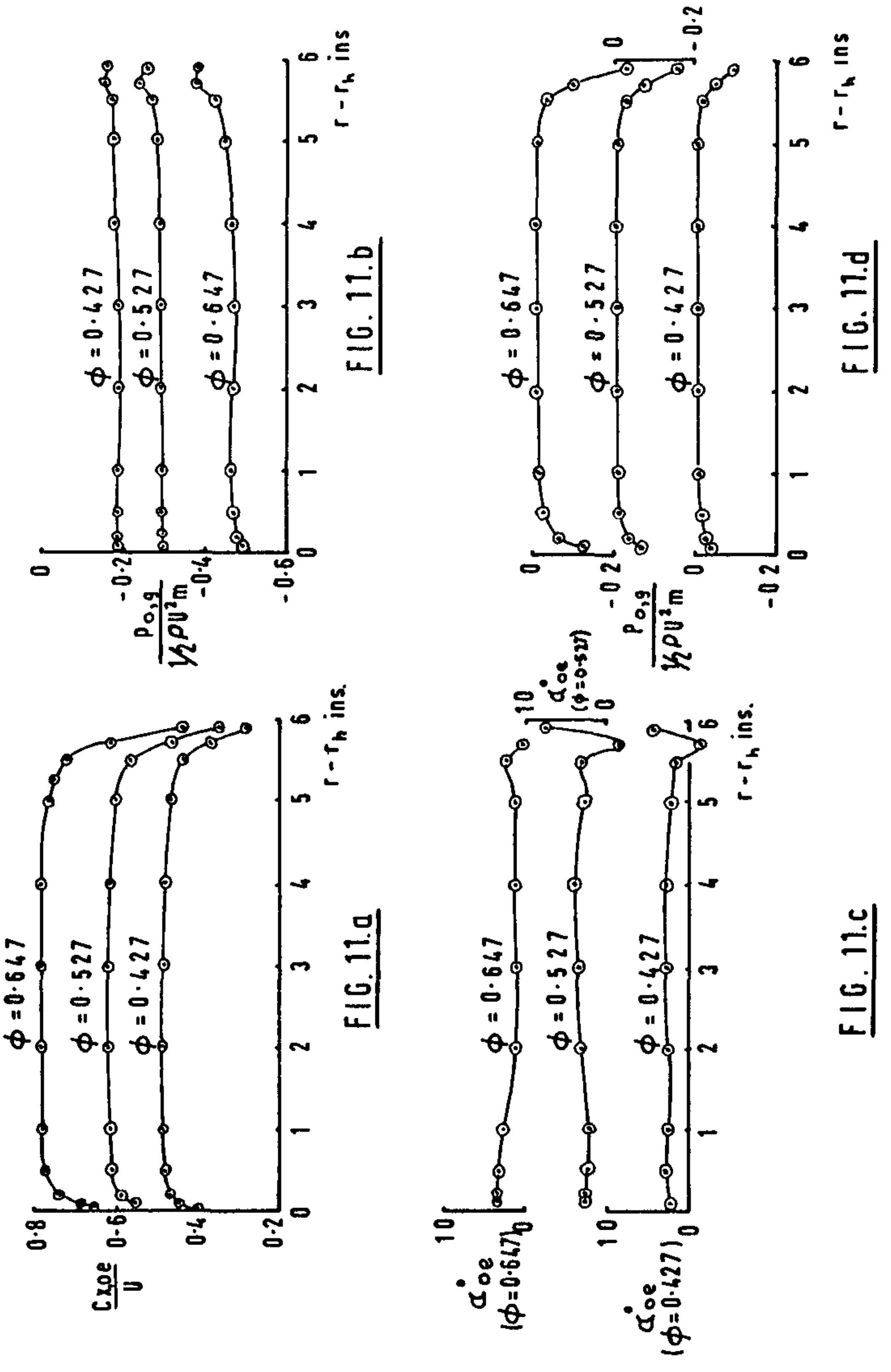
FIG. 11.a

FIG. 11.b

FIG. 11.c

FIG. 11.d

FIG. 11. CONDITIONS AT ENTRY TO COMPRESSOR STAGE

(A.R. = 1·0)

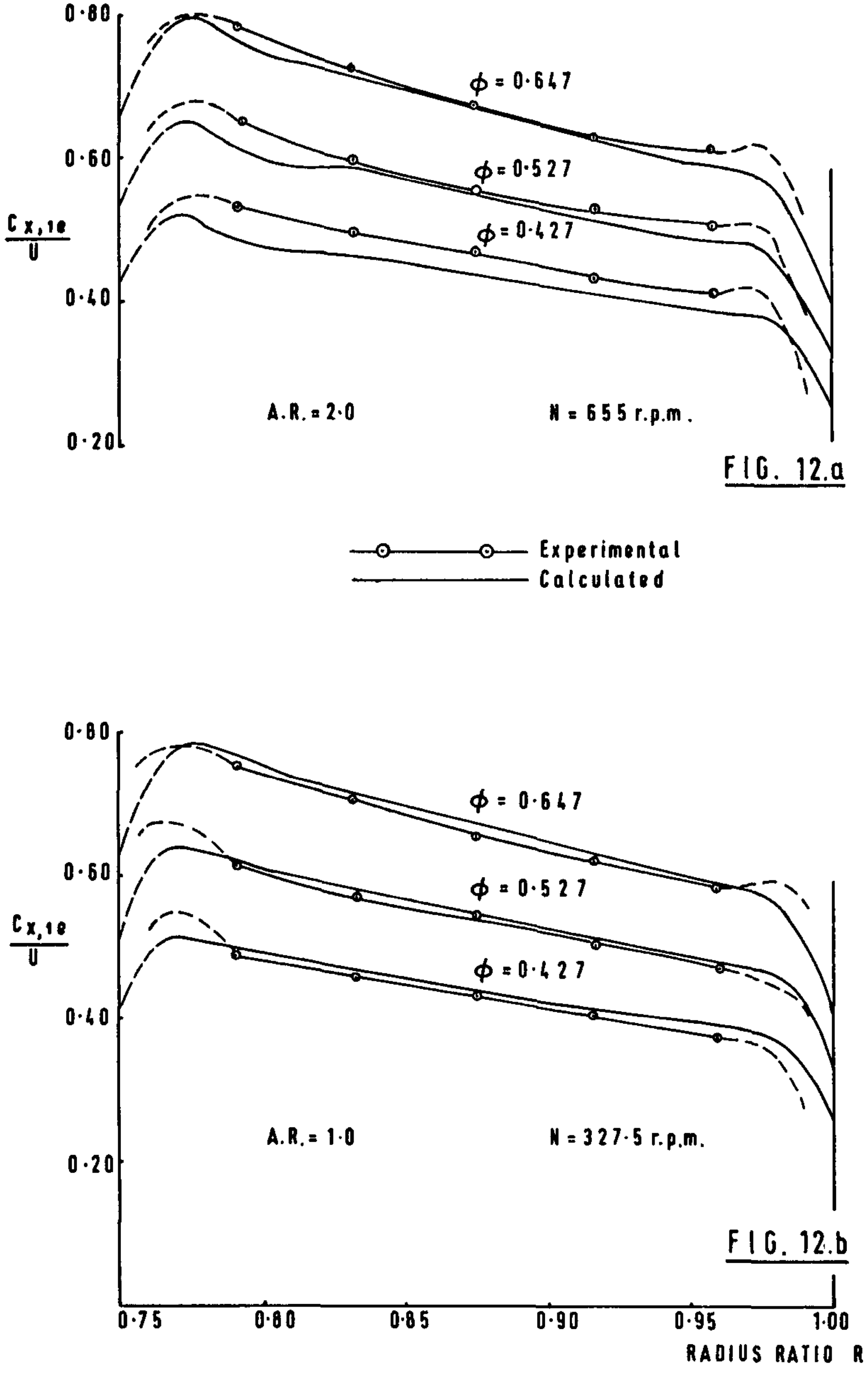

FIG. 12.a

FIG. 12.b

FIGS. 12.a,b AXIAL VELOCITY PROFILES AT I.G.V. TRAILING EDGE

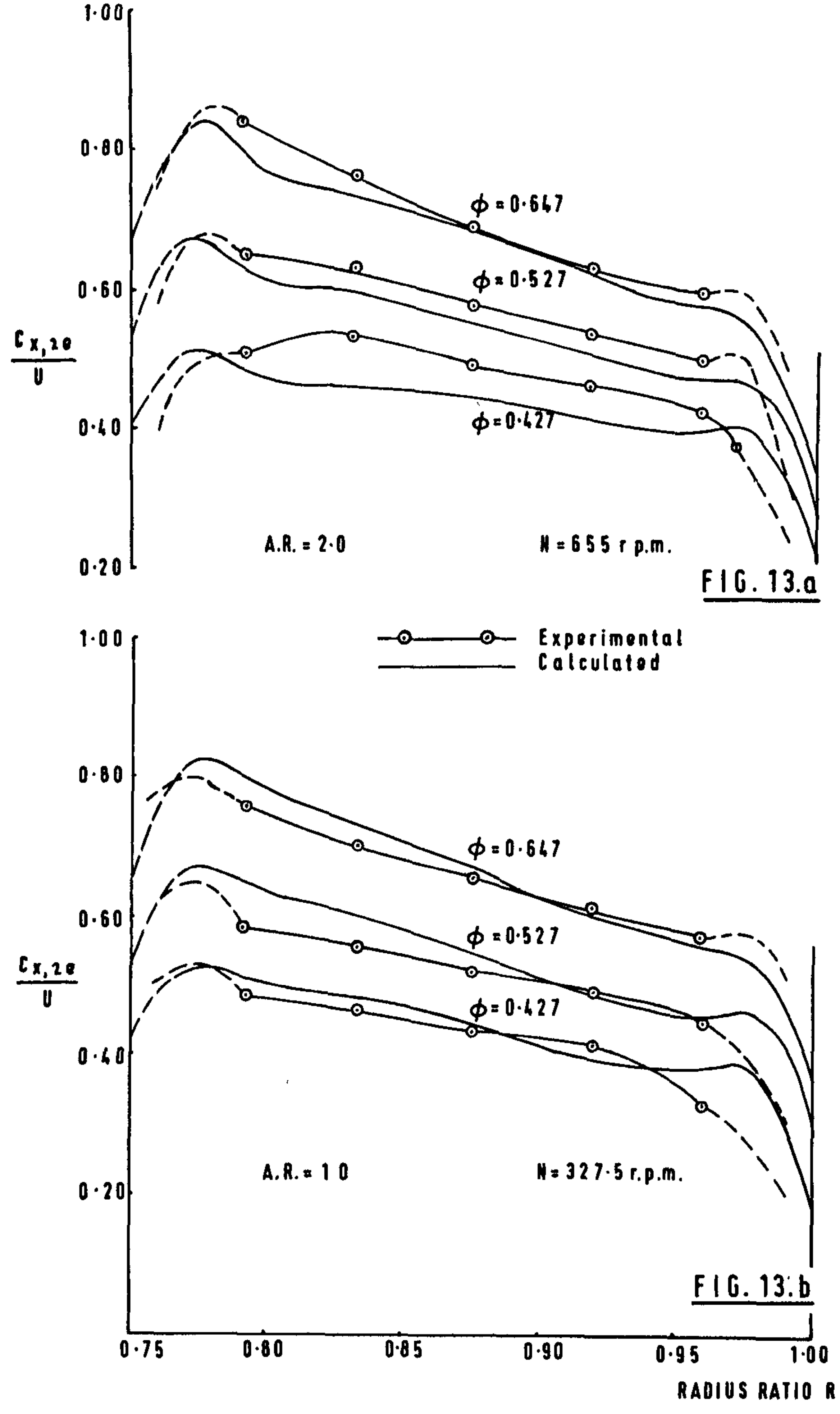

FIG. 13.a

FIG. 13.b

FIGS 13.a,b AXIAL VELOCITY PROFILES AT ROTOR TRAILING EDGE

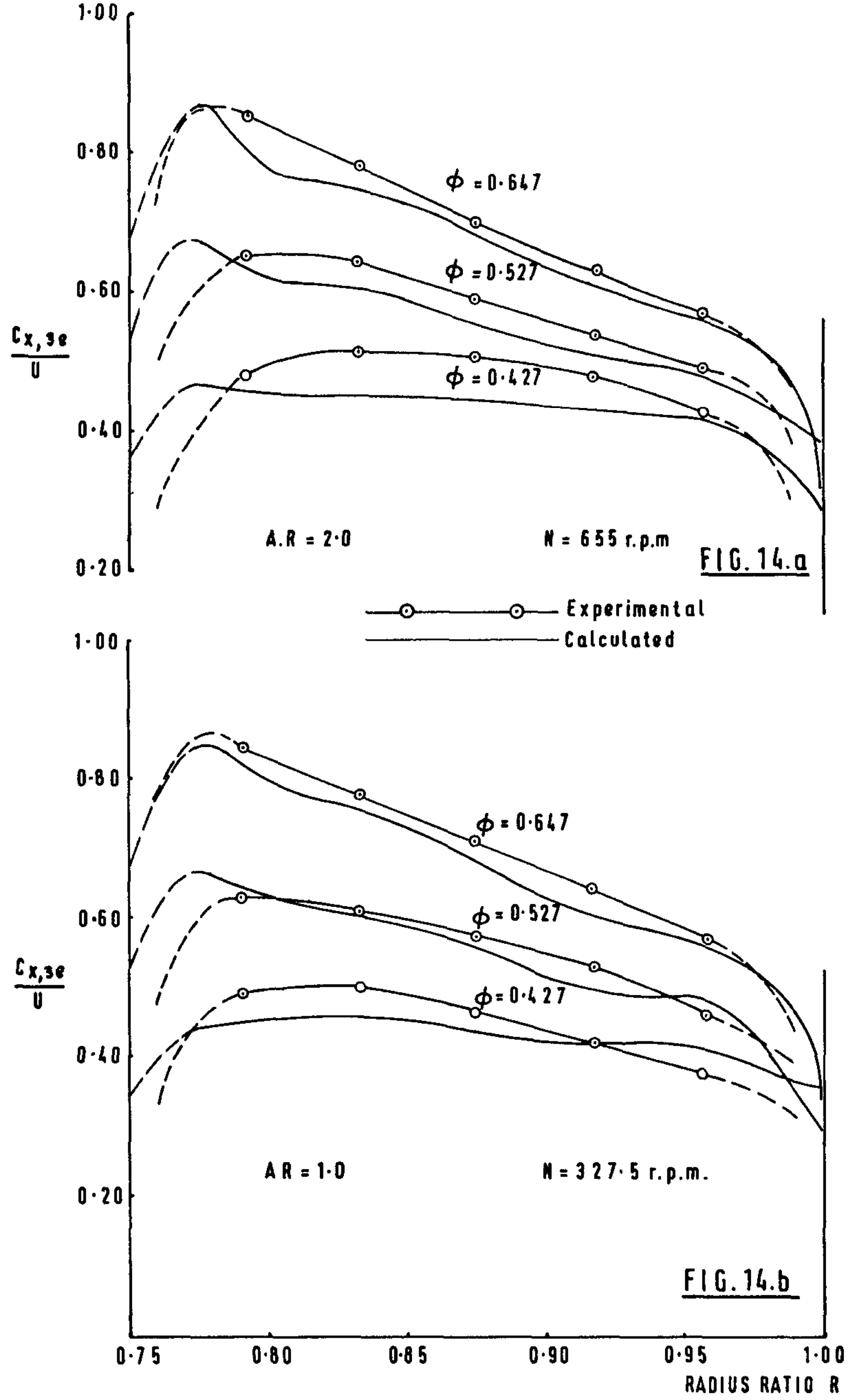

FIGS. 14.a,b AXIAL VELOCITY PROFILES AT STATOR TRAILING EDGE

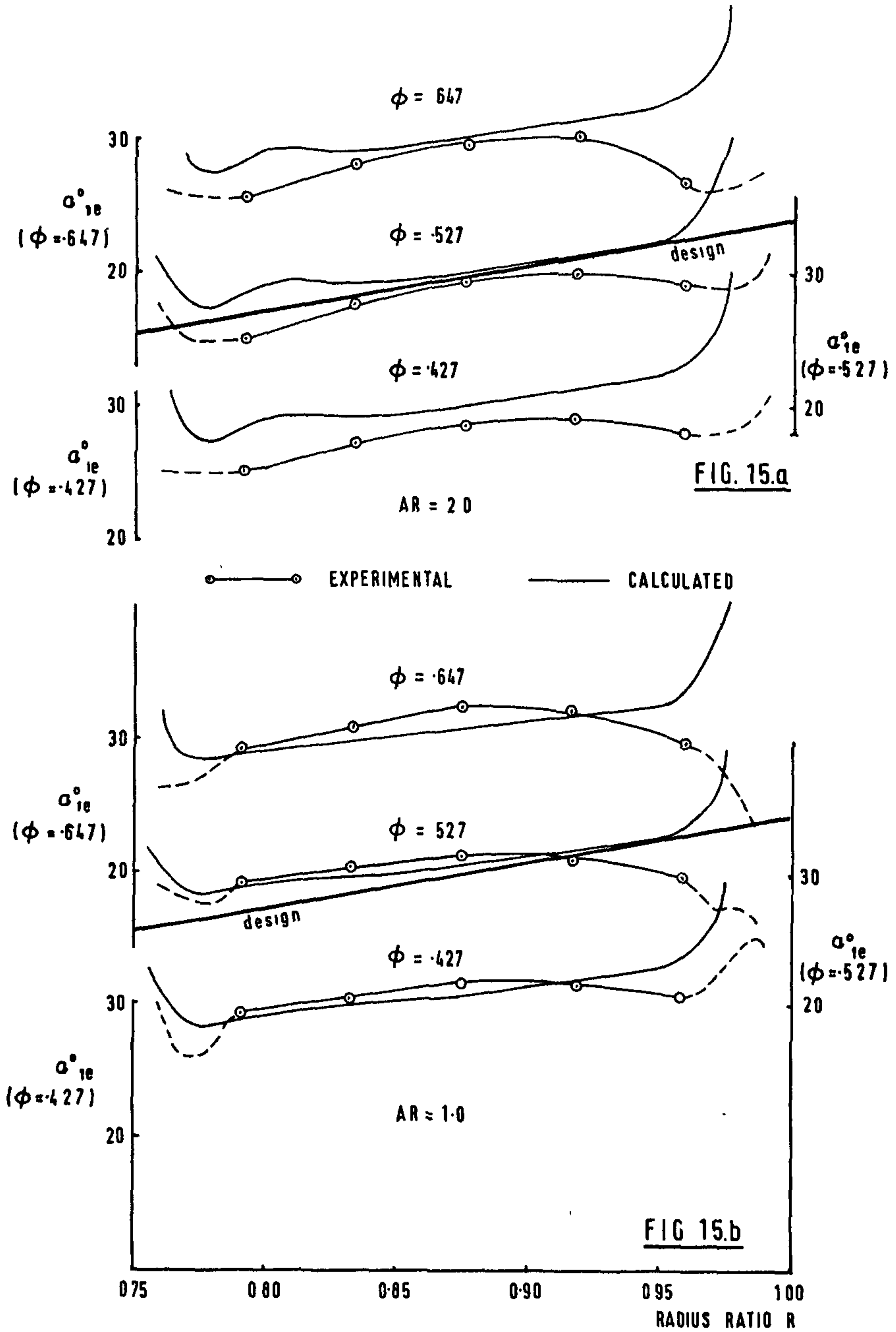

FIG. 15.a

FIG 15.b

FIGS 15.a,b ABSOLUTE AIR ANGLES AT I.G.V. TRAILING EDGE

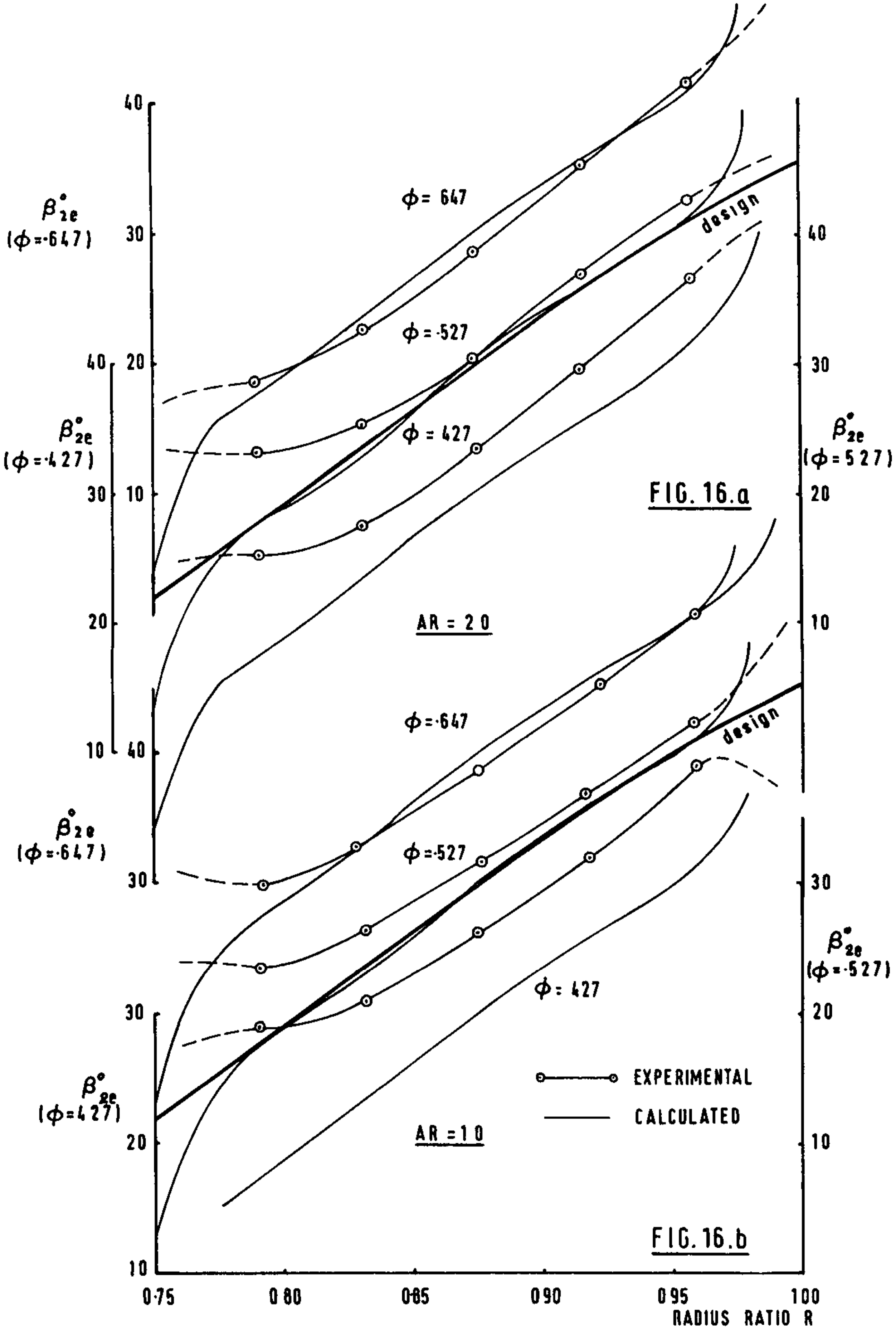

FIG. 16.a

FIG. 16.b

FIGS. 16a,b RELATIVE AIR ANGLES AT ROTOR TRAILING EDGE

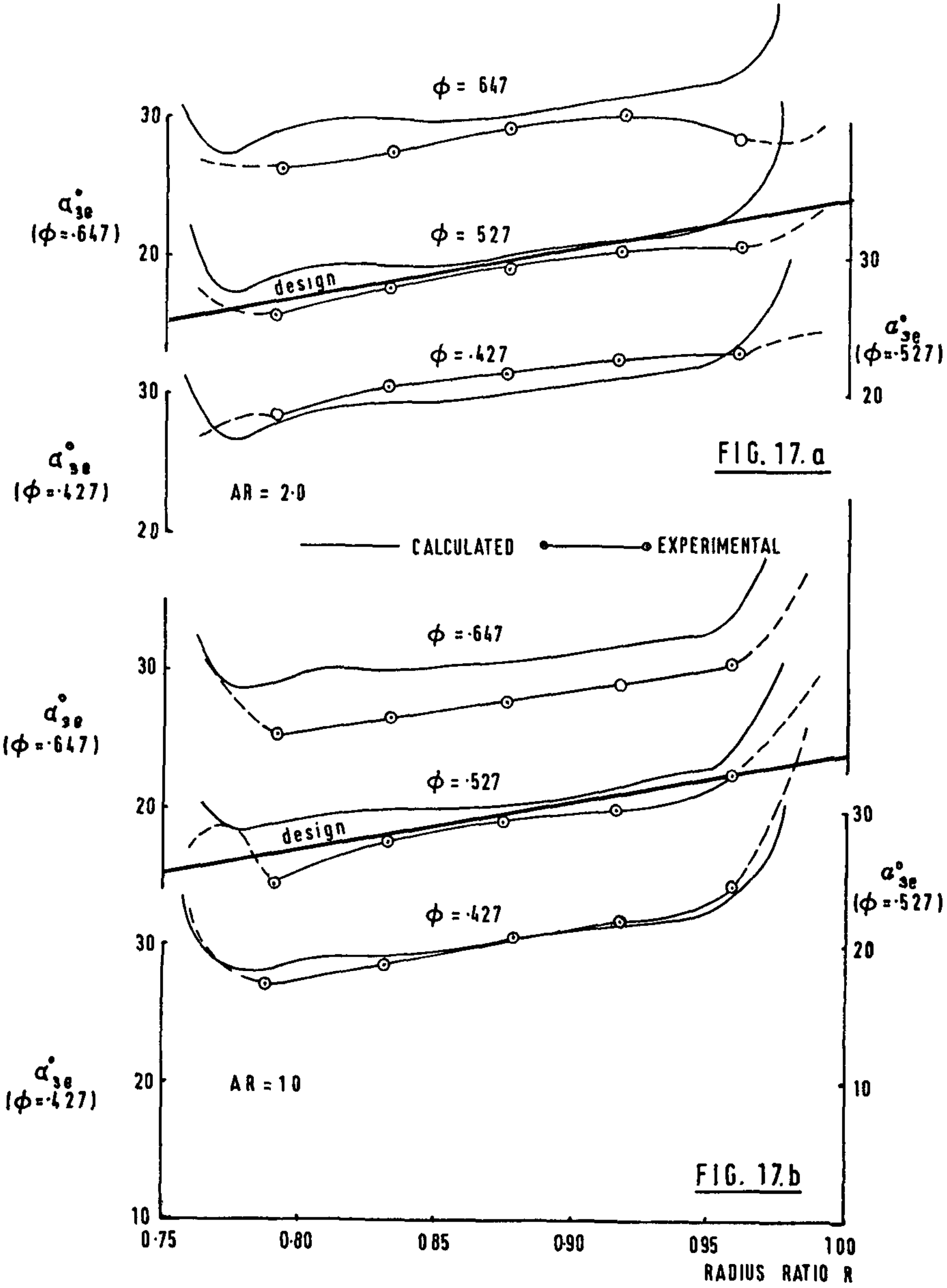

FIGS. 17.a,b ABSOLUTE AIR ANGLES AT STATOR TRAILING EDGE

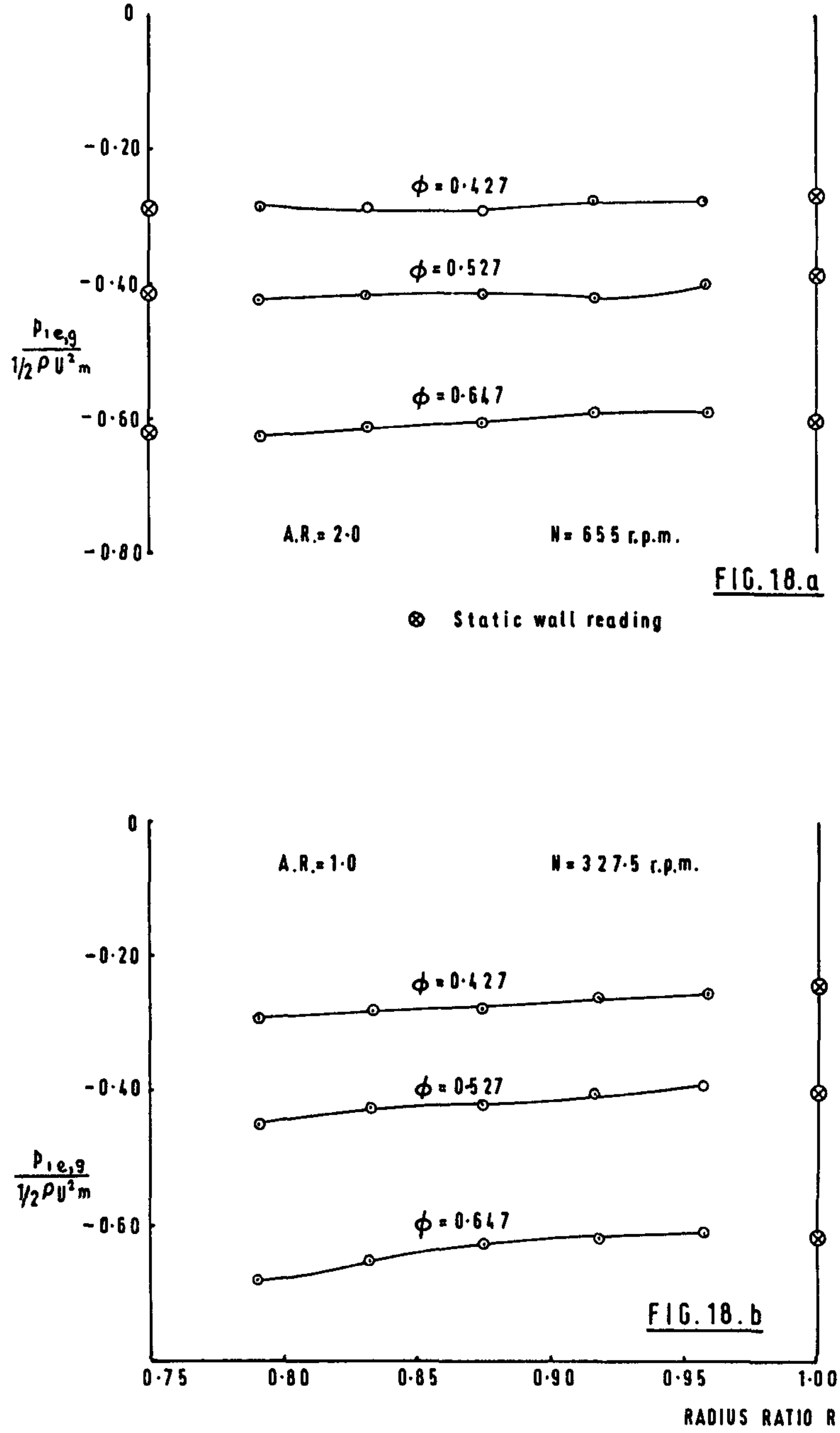

FIG. 18.a

FIG. 18.b

FIGS. 18.a,b STATIC PRESSURES AT I.G.V. TRAILING EDGE

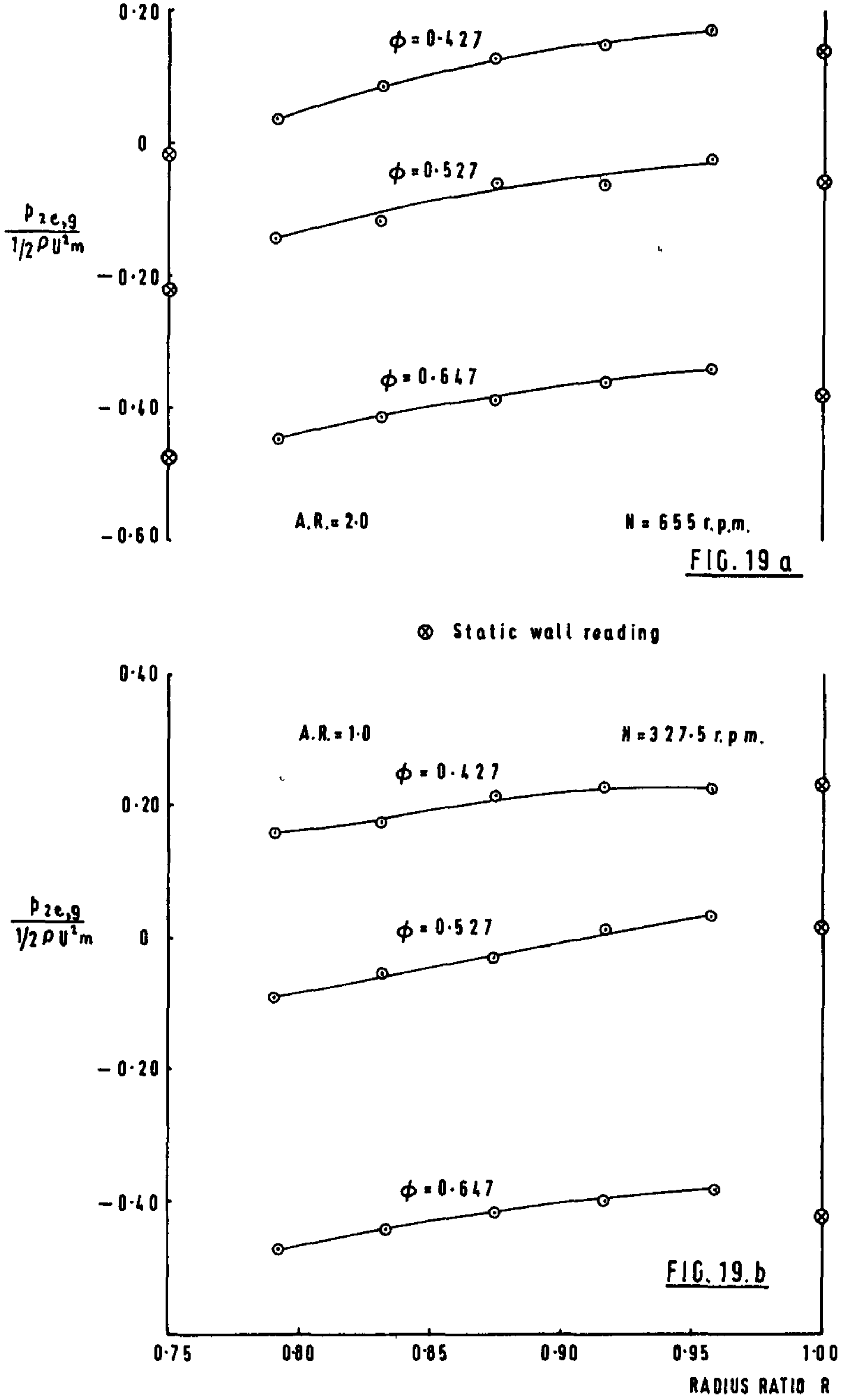

FIG. 19 a

FIG. 19.b

FIGS. 19.a,b STATIC PRESSURES AT ROTOR TRAILING EDGE

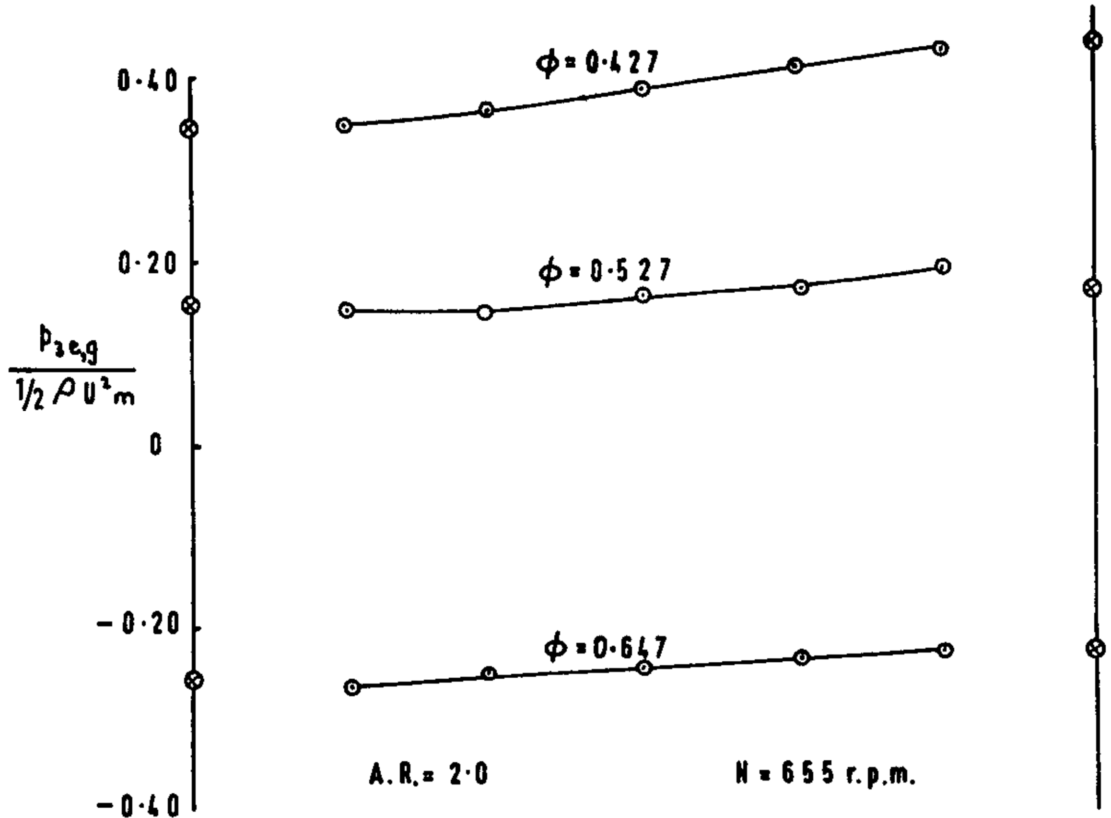

FIG 20.a

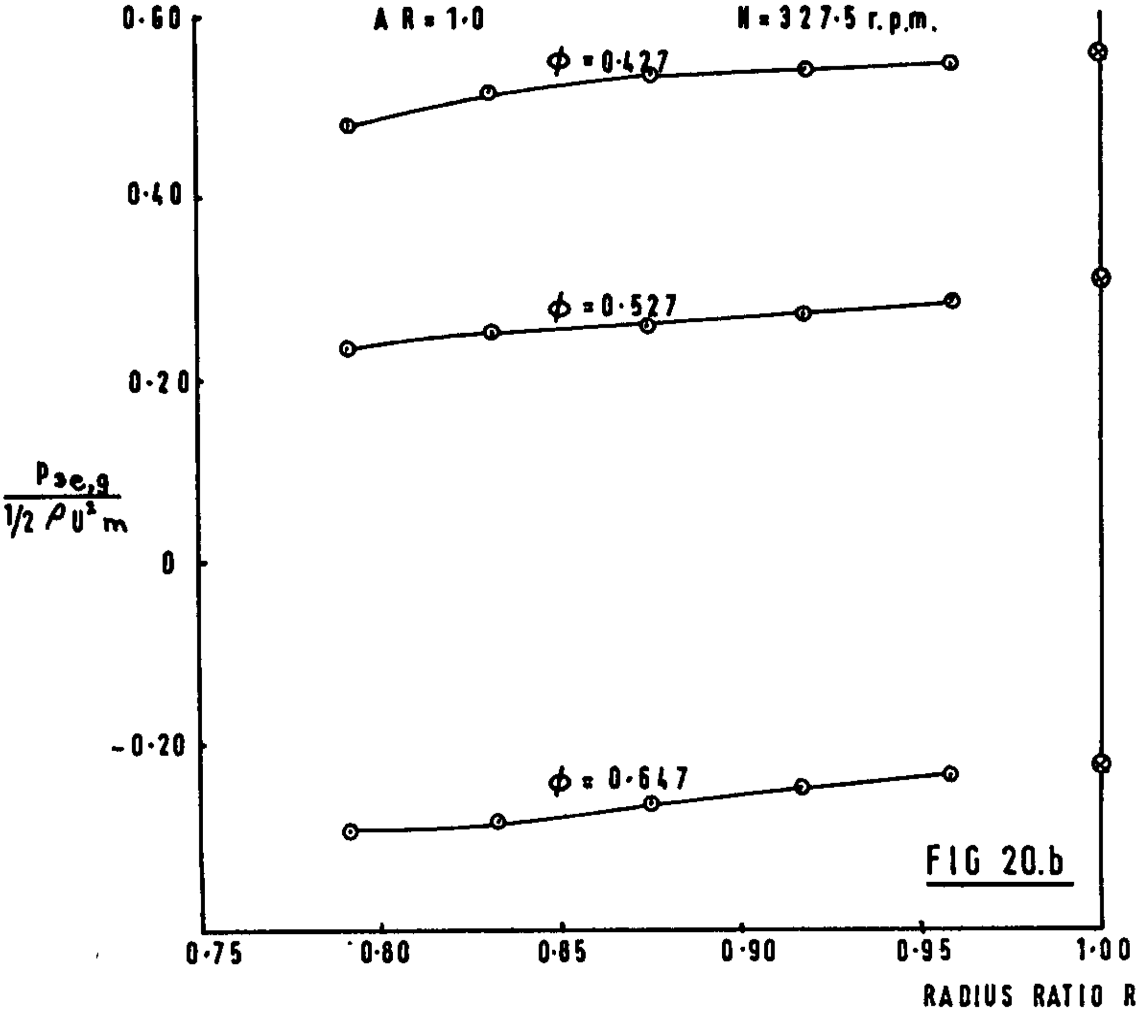

FIG 20.b

FIGS 20.a, b STATIC PRESSURES AT STATOR TRAILING EDGE

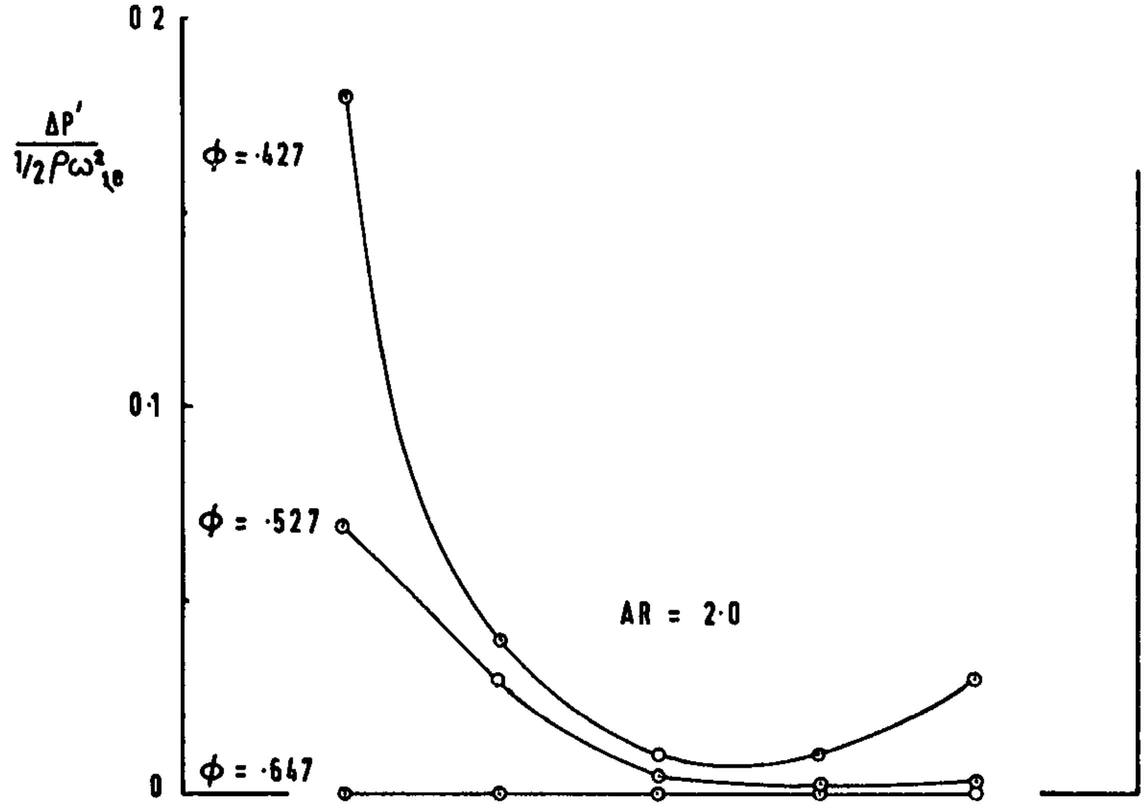

FIG. 21.a

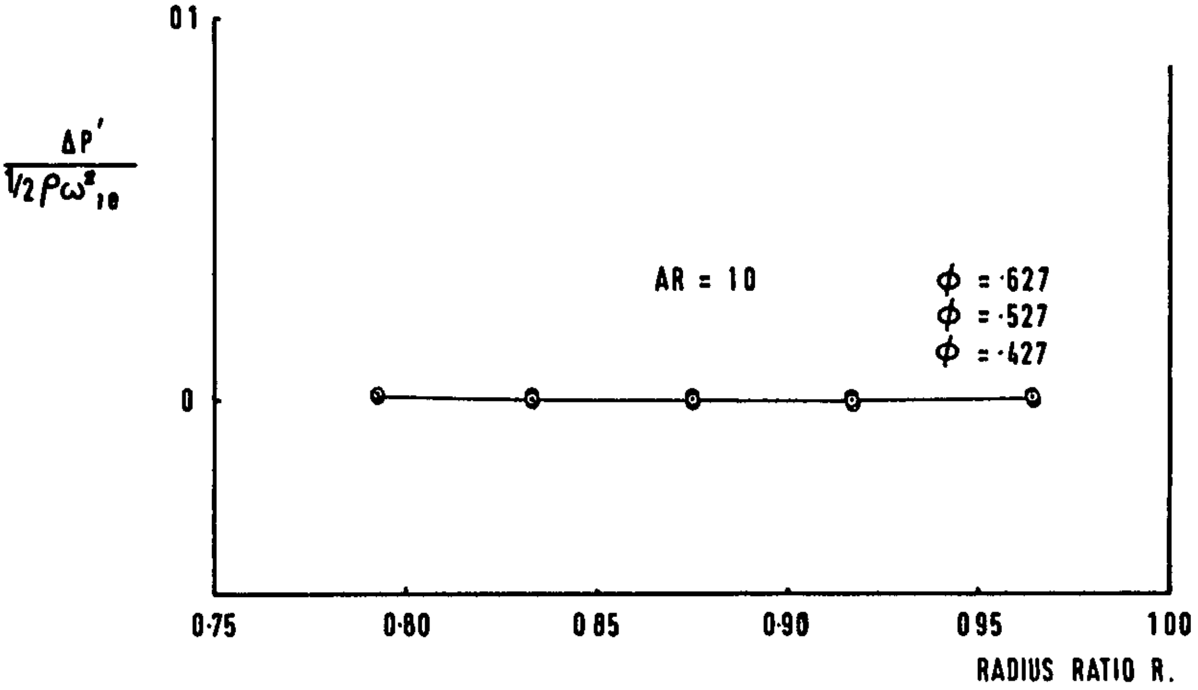

FIG. 21.b

FIG. 21.a,b RELATIVE TOTAL PRESSURE LOSS COEFFICIENT ACROSS ROTOR

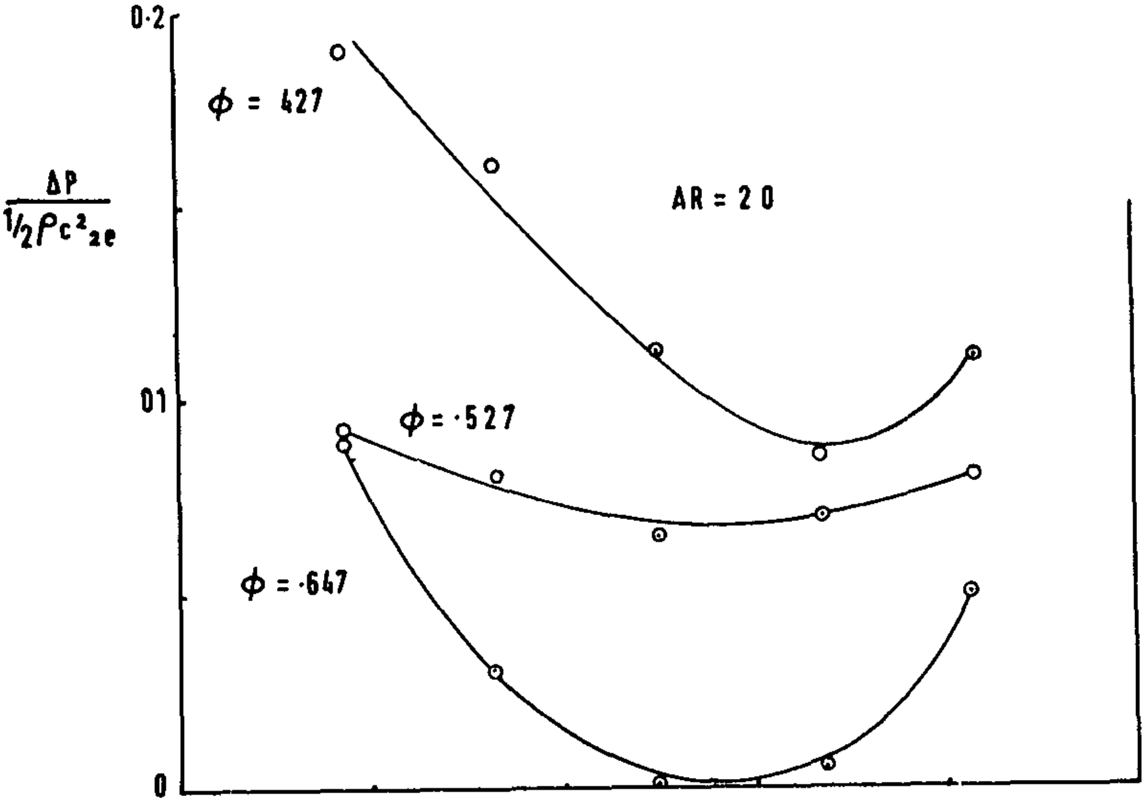

FIG. 22.a

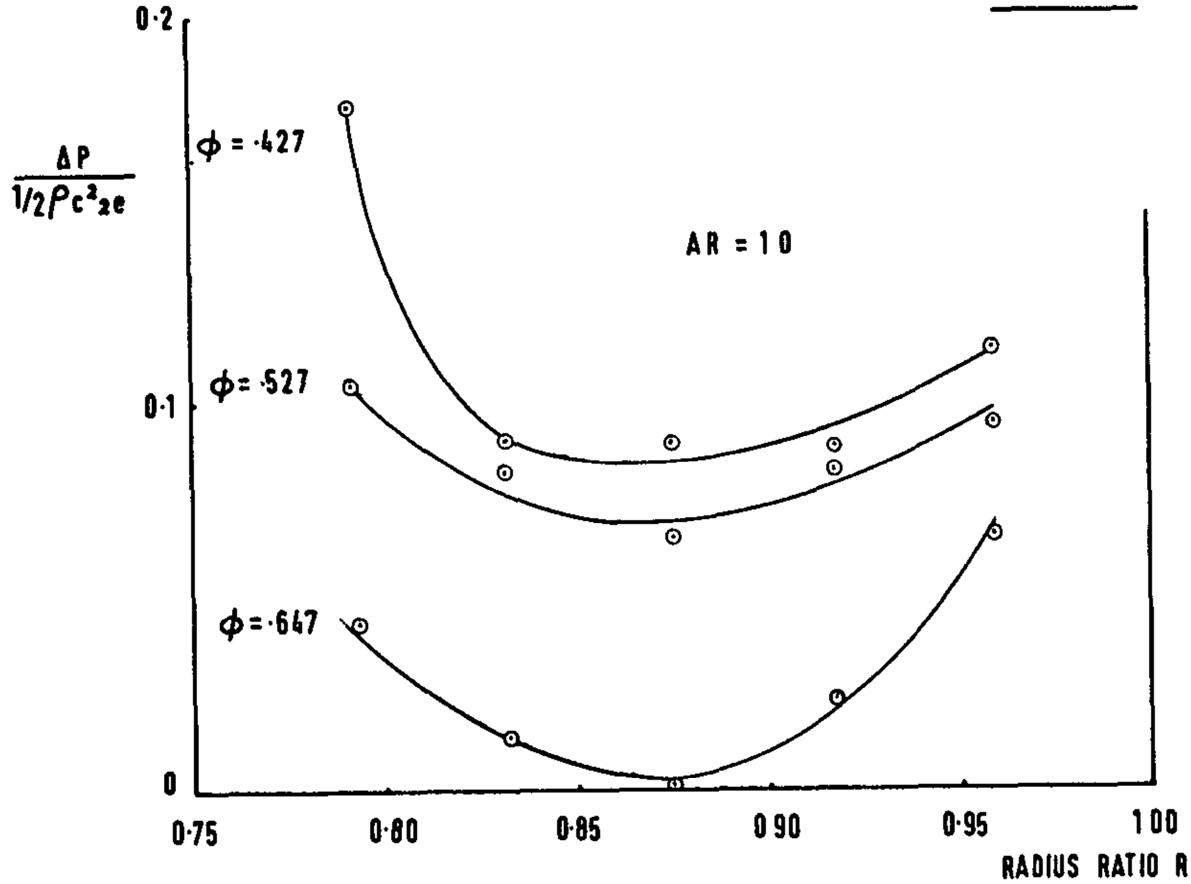

FIG. 22.b

FIG. 22.a,b ABSOLUTE TOTAL PRESSURE LOSS COEFFICIENT ACROSS STATOR

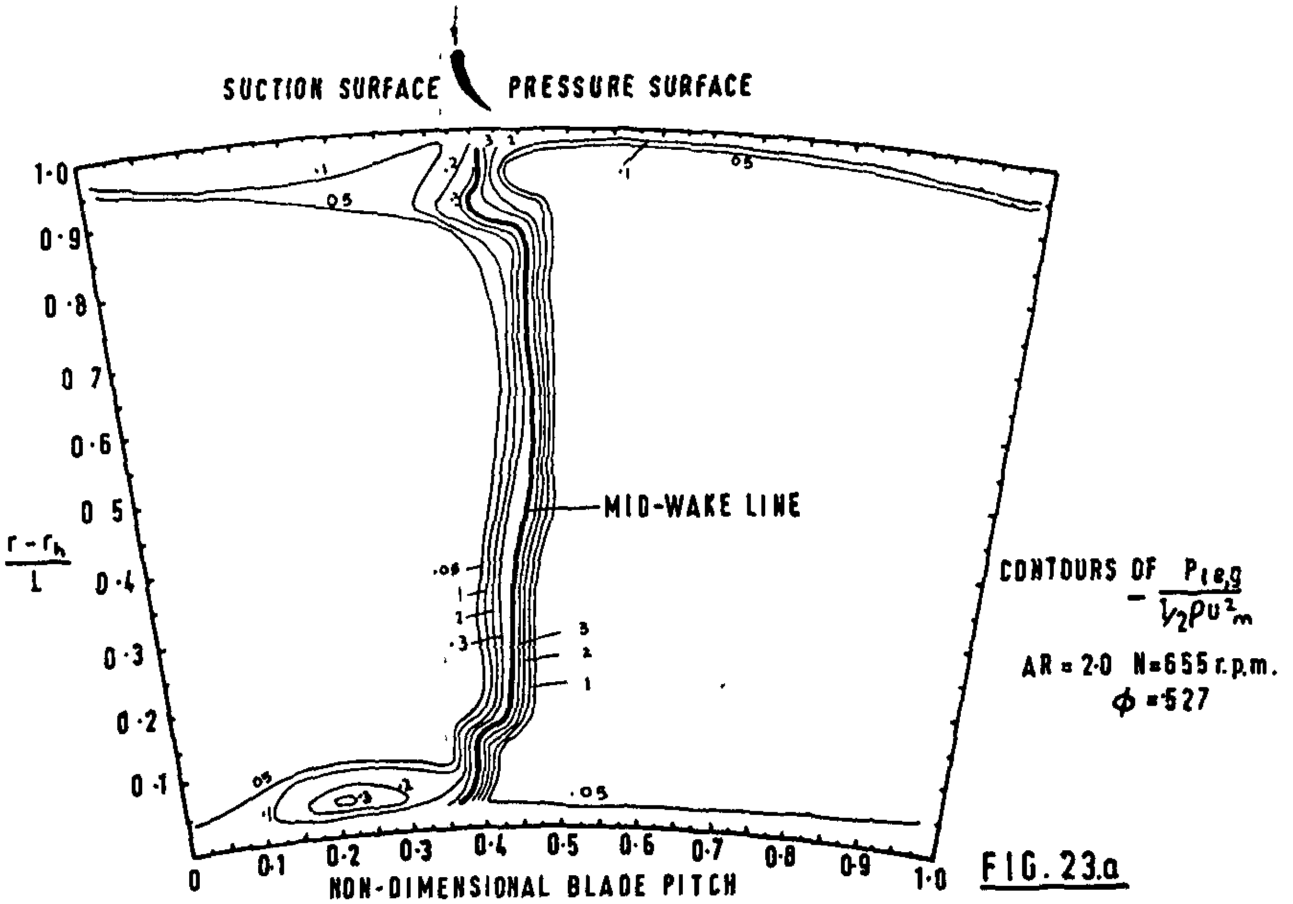

FIG. 23.a

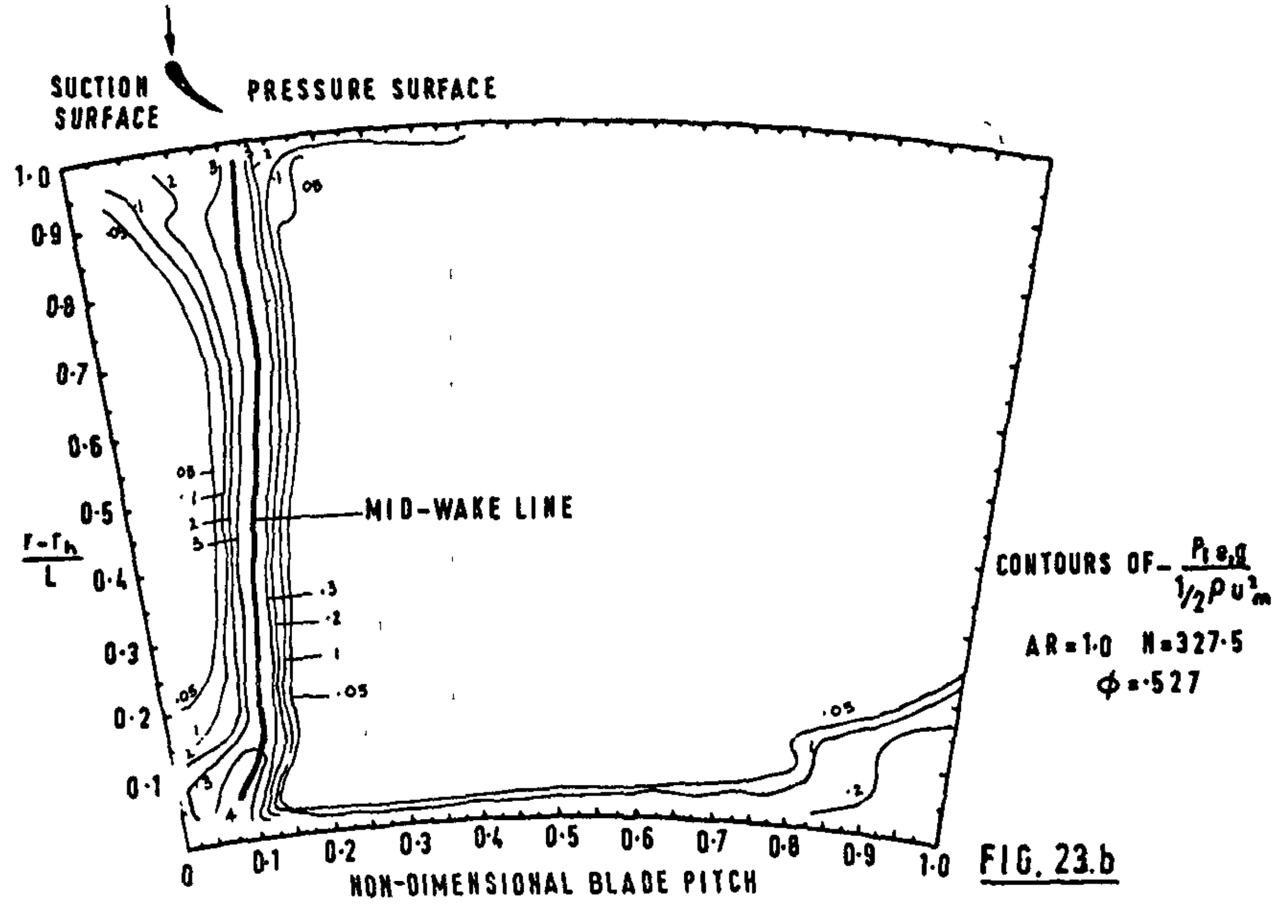

FIG. 23.b

FIGS. 23.a,b TOTAL PRESSURE CONTOURS AT I.G.V. TRAILING EDGE

(AT-DESIGN)

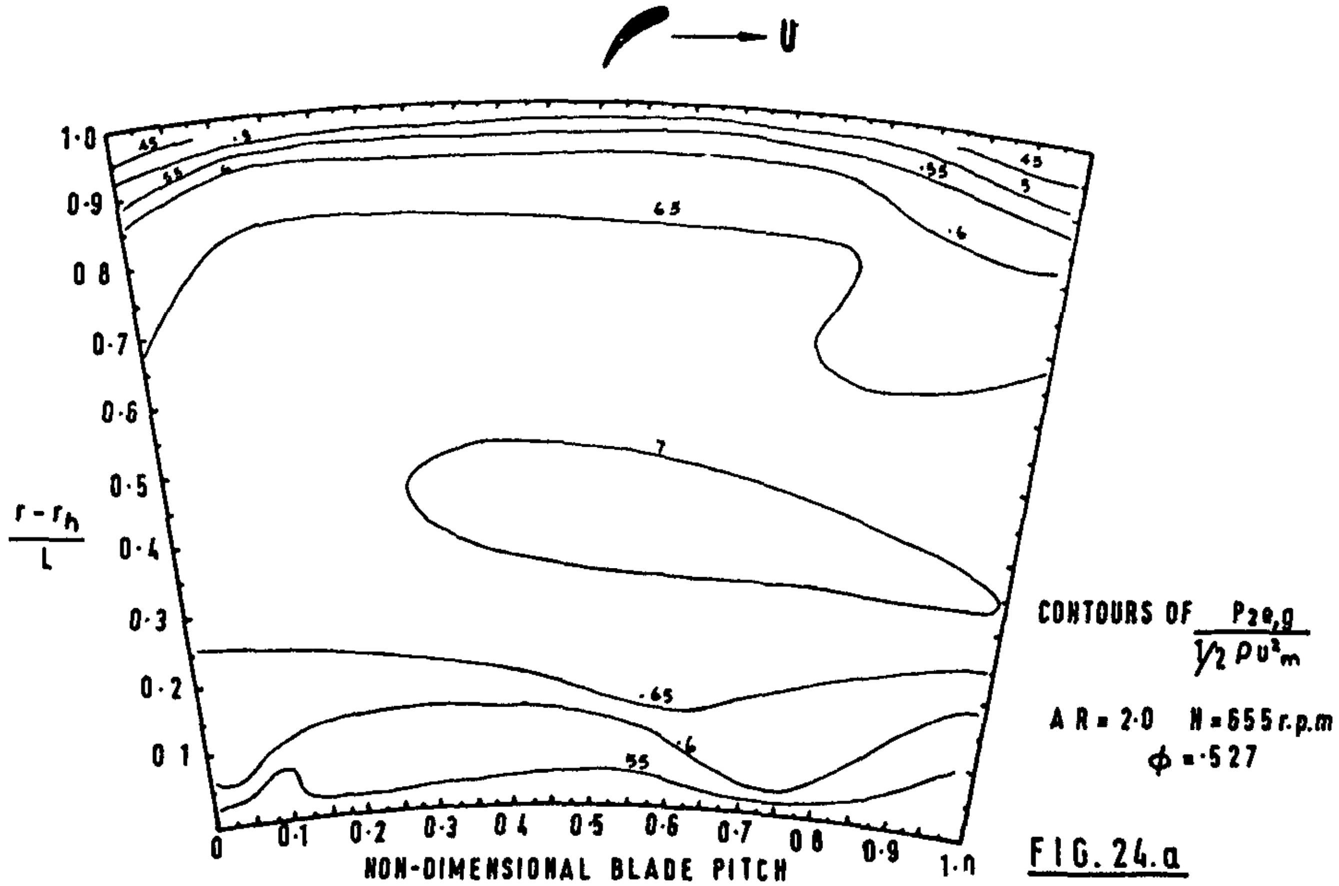

FIG. 24.a

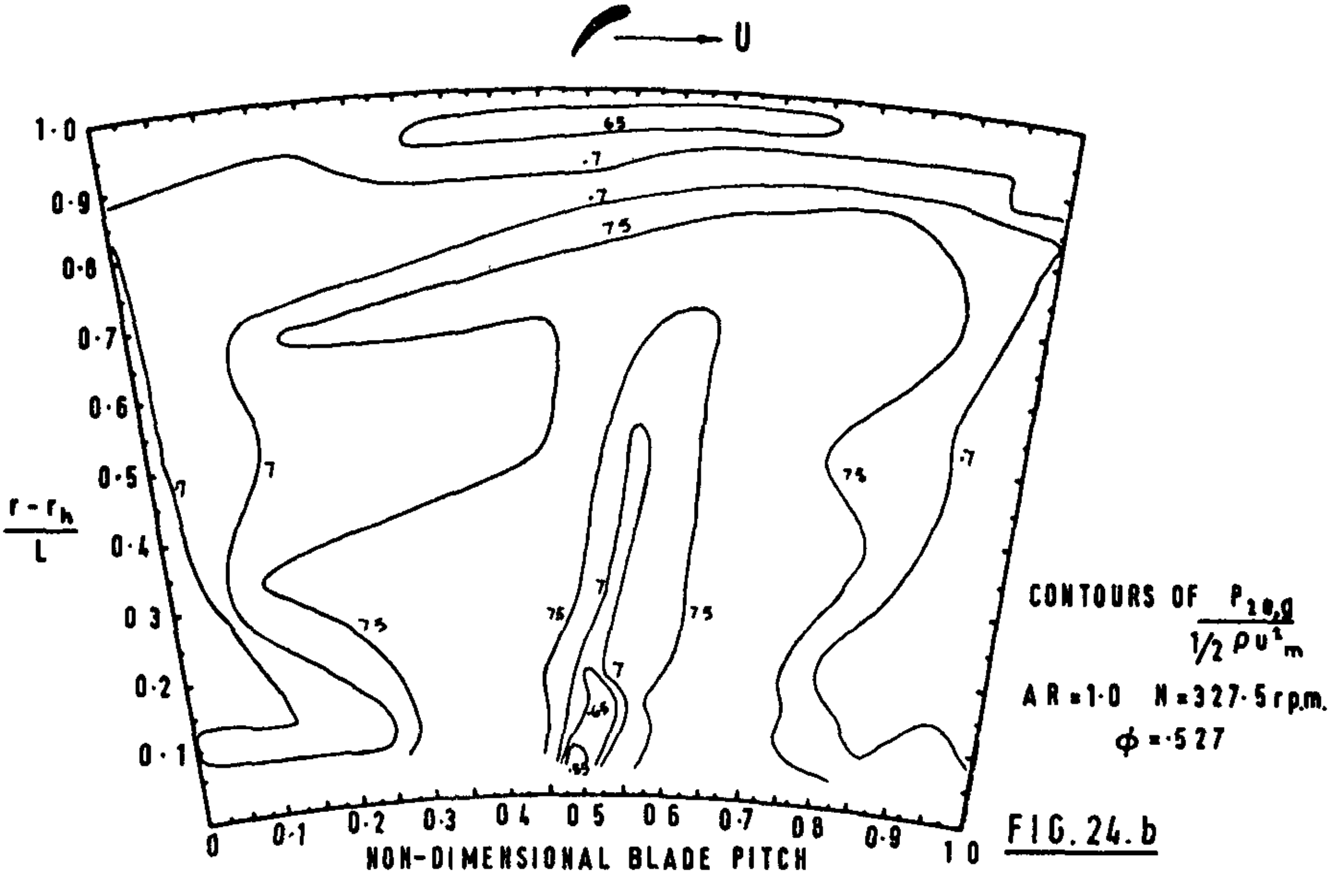

FIG. 24.b

FIGS 24 a,b TOTAL PRESSURE CONTOURS AT ROTOR TRAILING EDGE

(AT-DESIGN)

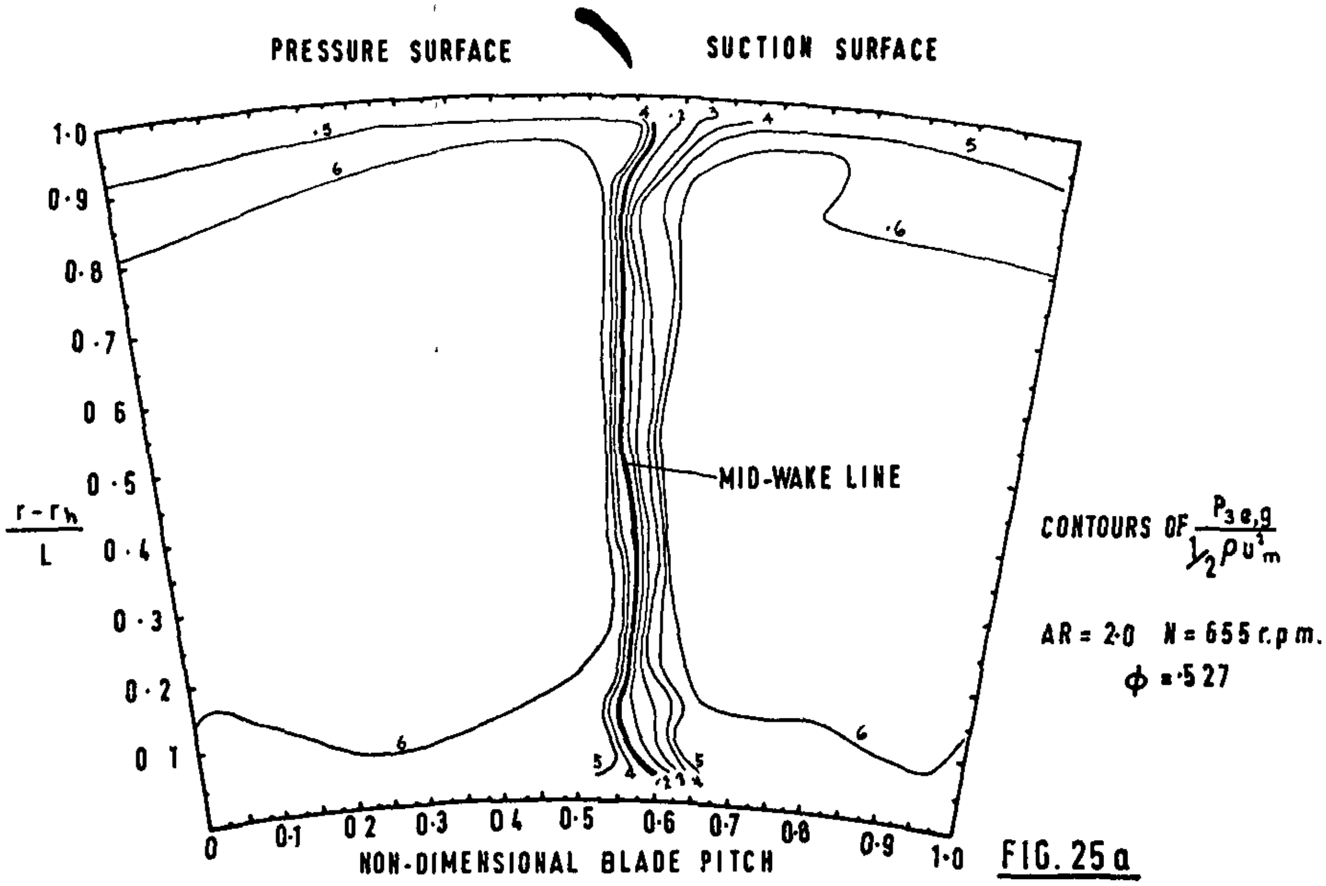

FIG. 25a

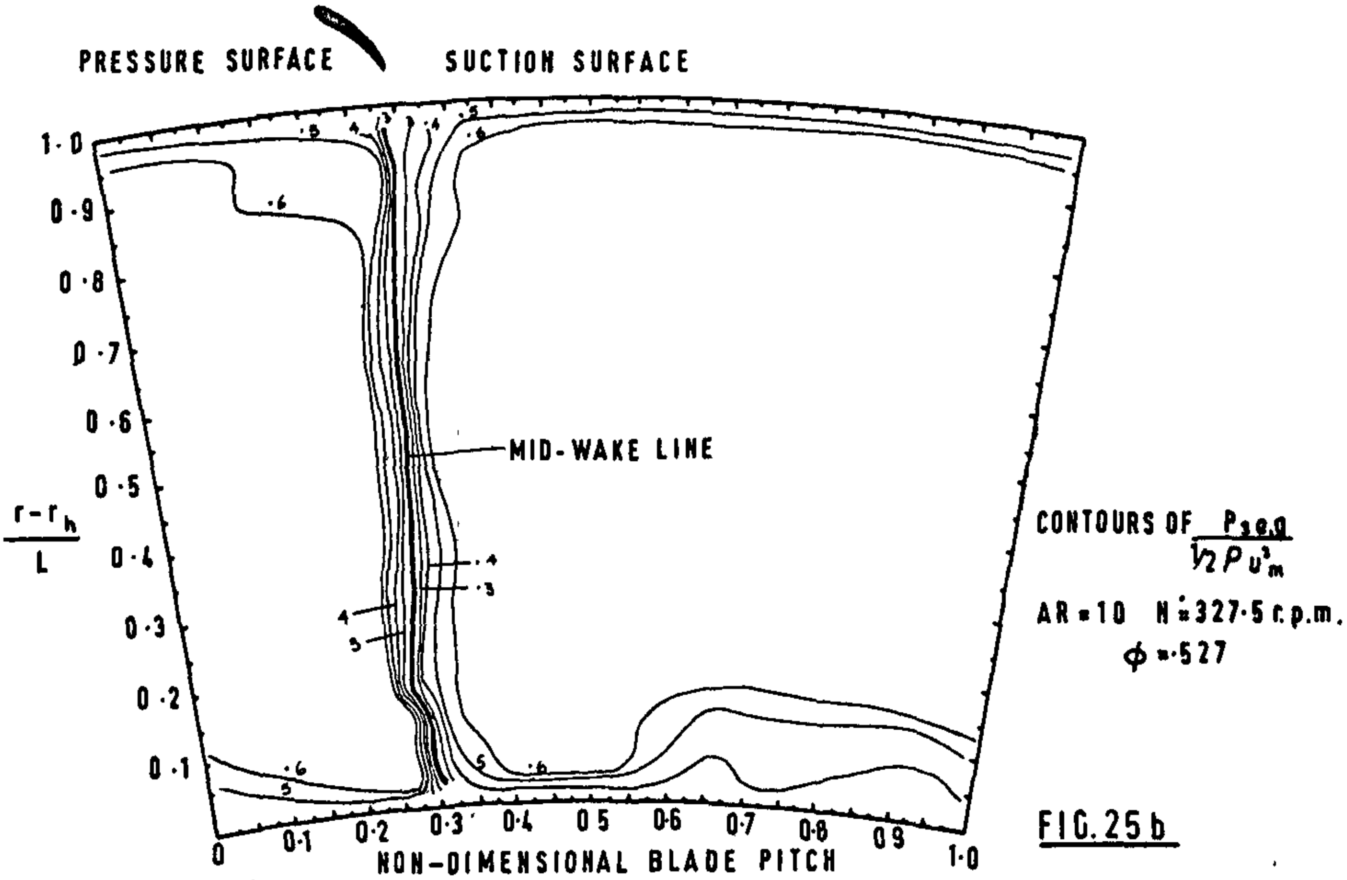

FIG. 25b

FIGS. 25a,b TOTAL PRESSURE CONTOURS AT STATOR TRAILING EDGE (AT-DESIGN)

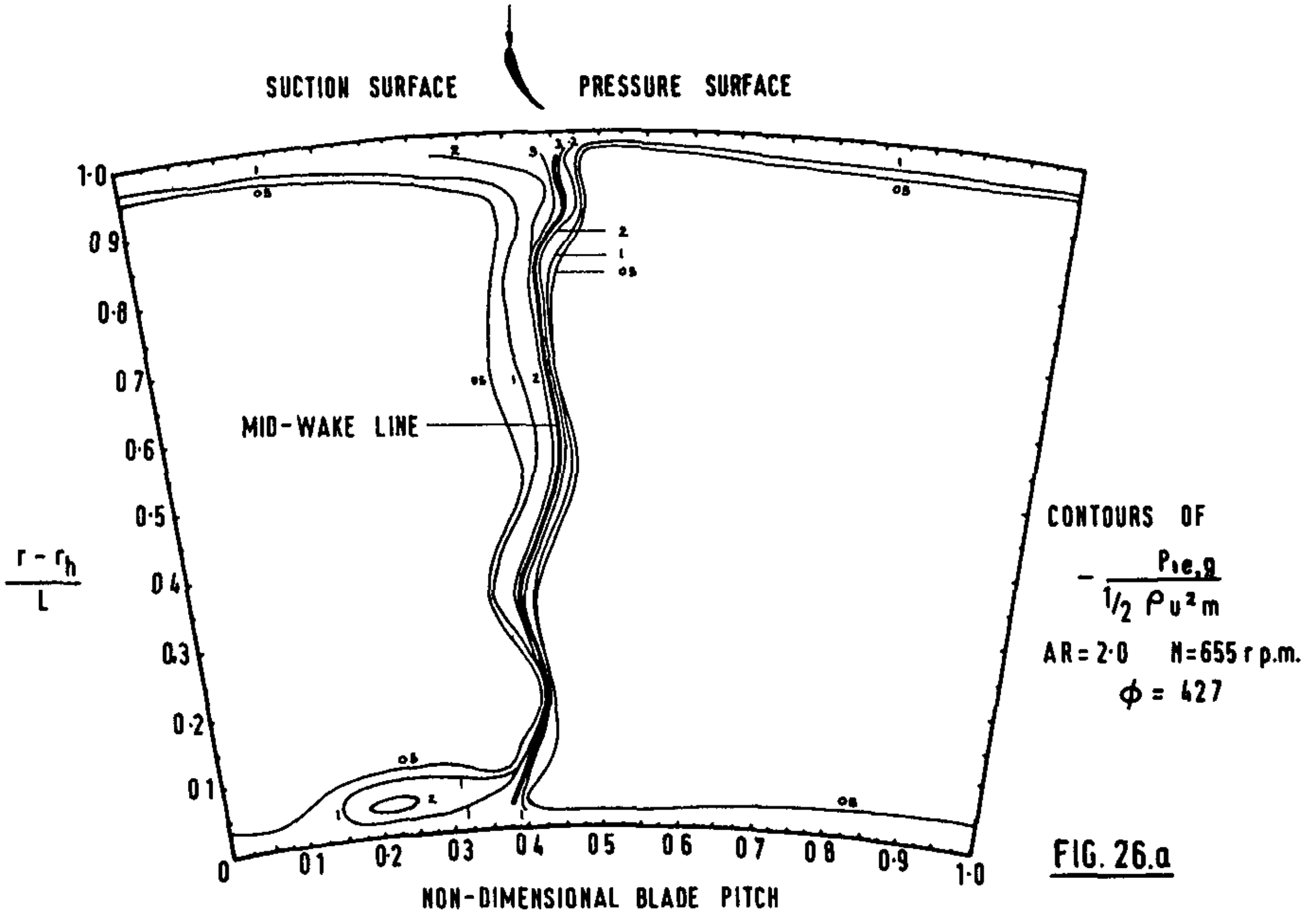

FIG. 26.a

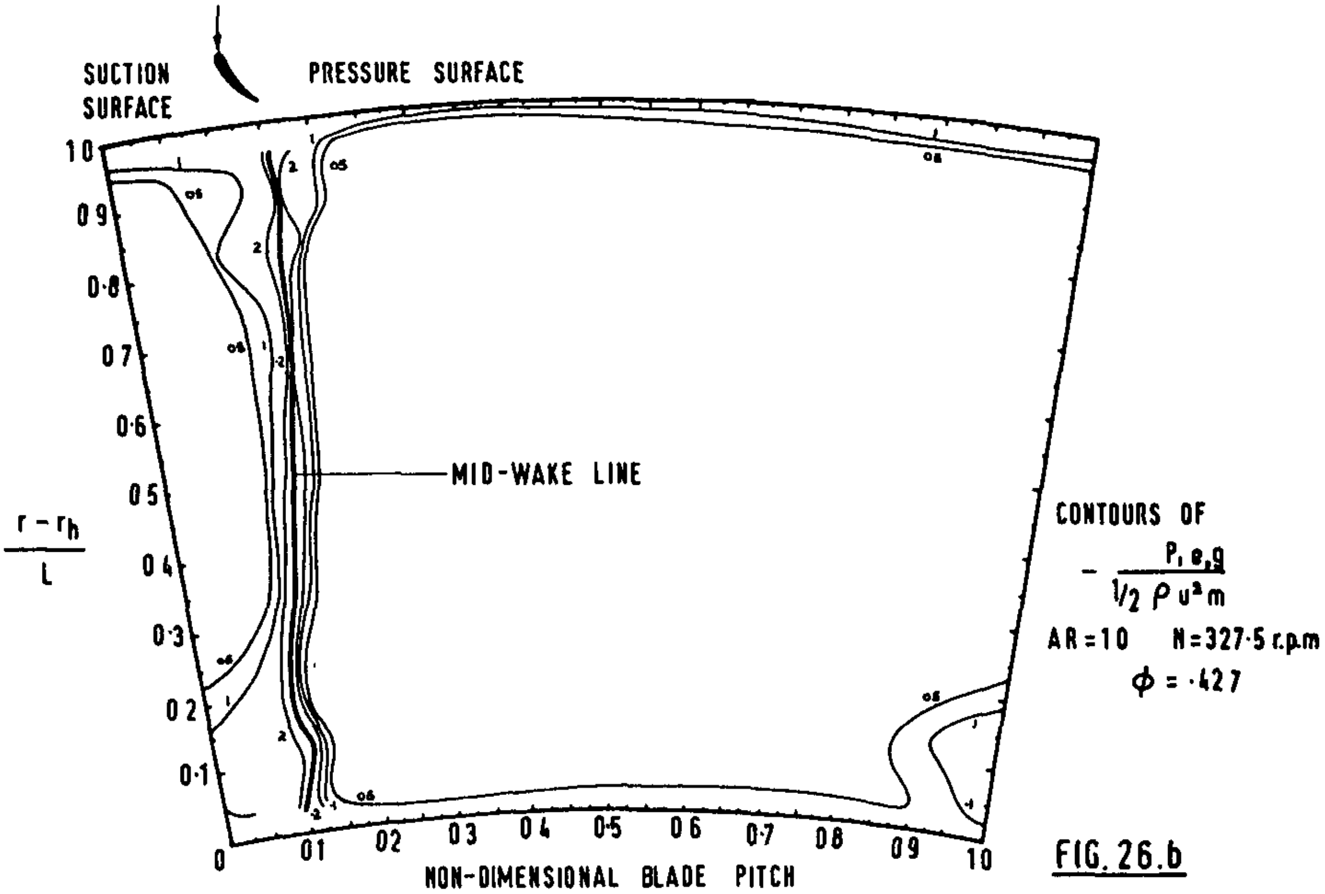

FIG. 26.b

FIGS 26 a,b TOTAL PRESSURE CONTOURS AT I.G.V. TRAILING EDGE (OFF-DESIGN)

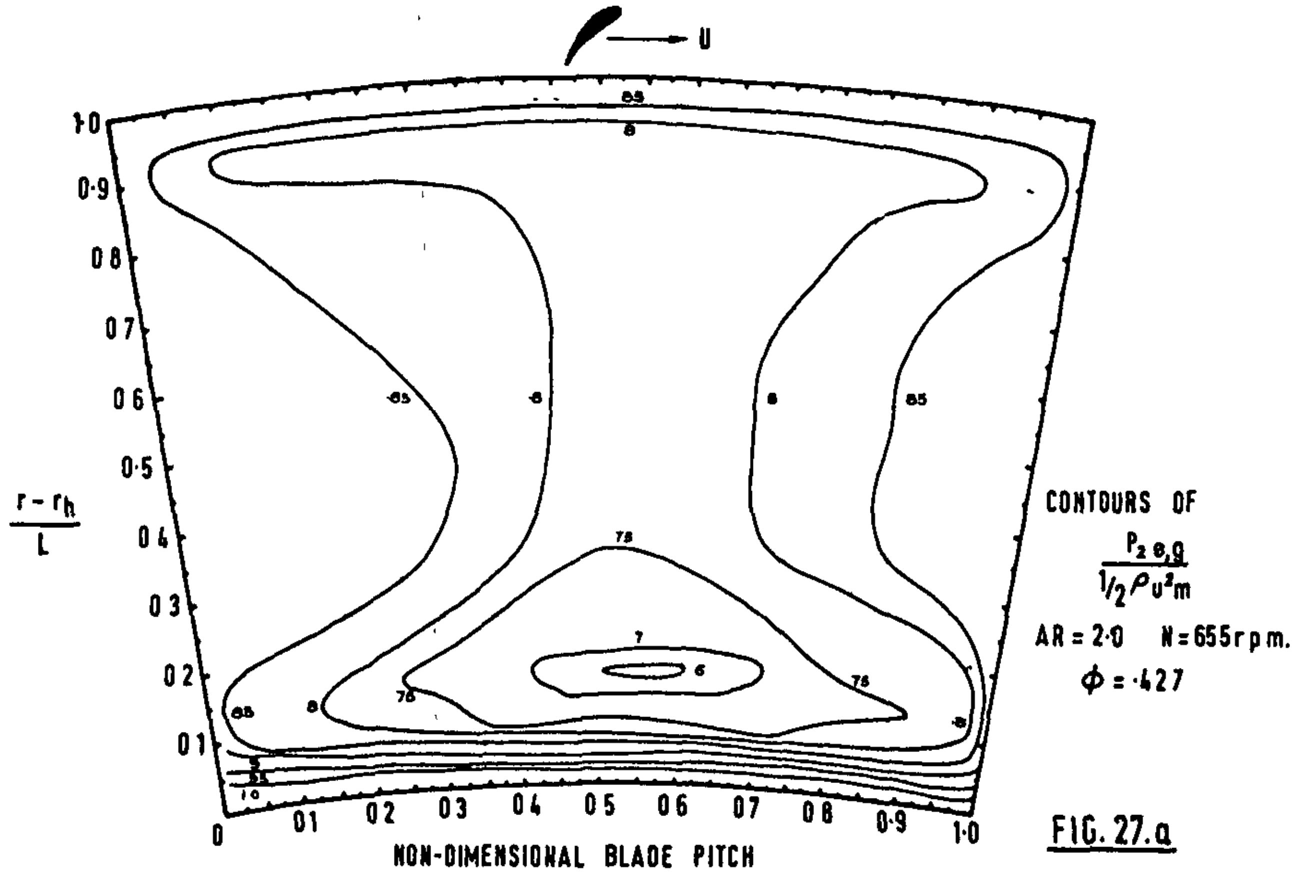

FIG. 27.a

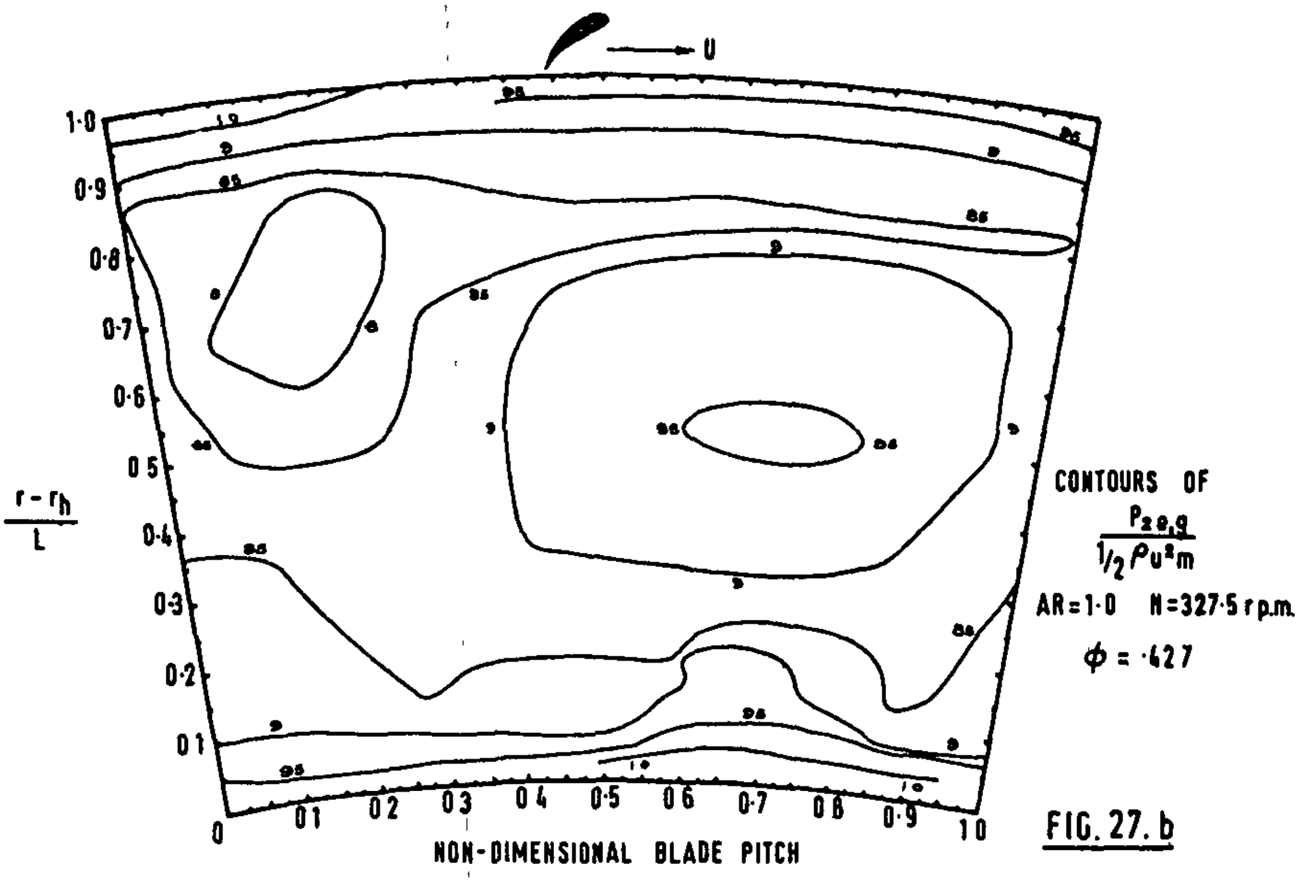

FIG. 27.b

FIGS 27.a b TOTAL PRESSURE CONTOURS AT ROTOR TRAILING EDGE (OFF-DESIGN)

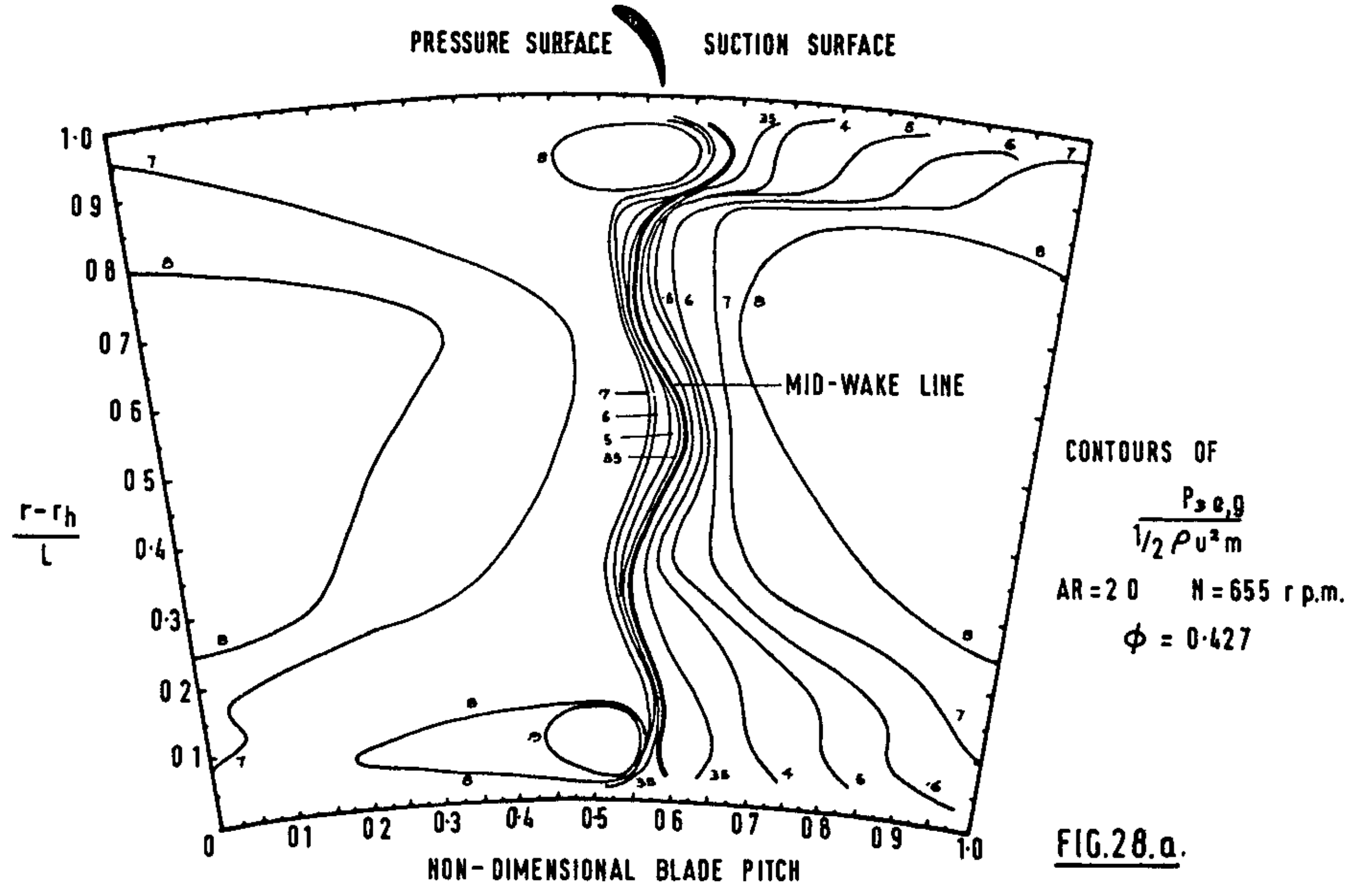

FIG.28.a.

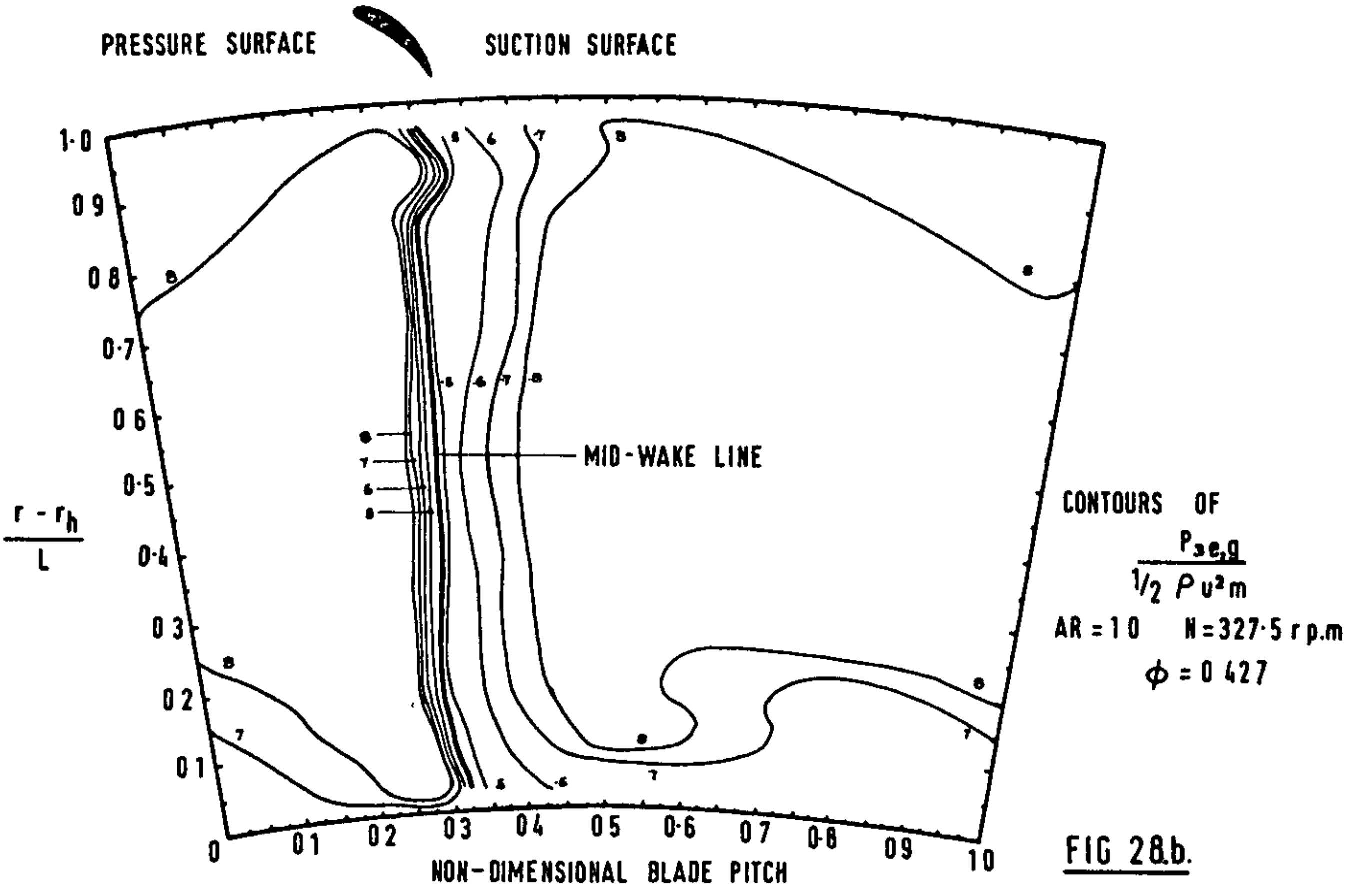

FIG 28.b.

FIGS 28a,b TOTAL PRESSURE CONTOURS AT STATOR TRAILING EDGE (OFF-DESIGN)

TABLE I BLADE DESIGN GEOMETRY

α'_1 (INLET ANGLE) α'_2 (OUTLET ANGLE) θ (CAMBER ANGLE) λ (STAGGER ANGLE)

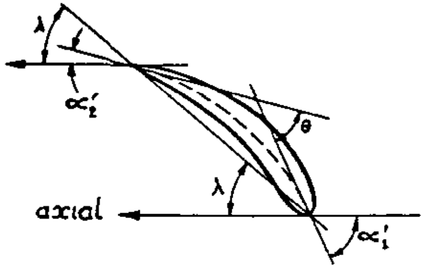

DESIGN	CHORD LENGTH (in)	ASPECT RATIO	PASSAGE HEIGHT (in)	NUMBER OF BLADES	BLADE PROFILE	ROTOR SPEED (r.p.m)	RADIAL POSITION	SPACE/CHORD RATIO	RADIUS (in)	RADIUS RATIO (R)	INLET GUIDE VANE				ROTOR				STATOR			
											DEGREES				DEGREES				DEGREES			
											α'_1	α'_2	θ	λ	α'_1	α'_2	θ	λ	α'_1	α'_2	θ	λ
CONSTANT SECTION BLADE	3·00	2·00	6·00	50	C4	655	HUB	0·754	18	0·750	57	35·7	30	20·7	51	21	30	36	51	21	30	36
							MEAN	0·879	21	0·875	"	"	"	"	"	"	"	"	"	"	"	"
							TIP	1·005	24	1·000	"	"	"	"	"	"	"	"	"	"	"	"
EXPONENTIAL (TWISTED) BLADE	3·00	2·00	6·00	50	C4	655	HUB	0·754	18	0·750	5·0	29·0	24·0	17·0	43·9	2·6	41·3	23·2	48·8	17·3	31·5	33·1
							MEAN	0·879	21	0·875	5·0	35·0	30·0	20·0	51·0	21·0	30·0	36·0	51·0	21·0	30·0	36·0
							TIP	1·005	24	1·000	5·0	41·1	36·1	23·1	57·4	40·8	16·6	49·1	53·9	25·6	28·2	39·8
EXPONENTIAL (TWISTED) BLADE	6·00	1·00	6·00	25	C4	327	HUB	0·752	18	0·750	5·0	29·0	24·0	17·0	43·9	2·6	41·3	23·2	48·8	17·3	31·5	33·1
							MEAN	0·877	21	0·875	5·0	35·0	30·0	20·0	51·0	21·0	30·0	36·0	51·0	21·0	30·0	36·0
							TIP	1·003	24	1·000	5·0	41·1	36·1	23·1	57·4	40·8	16·6	49·1	53·9	25·6	28·2	39·8

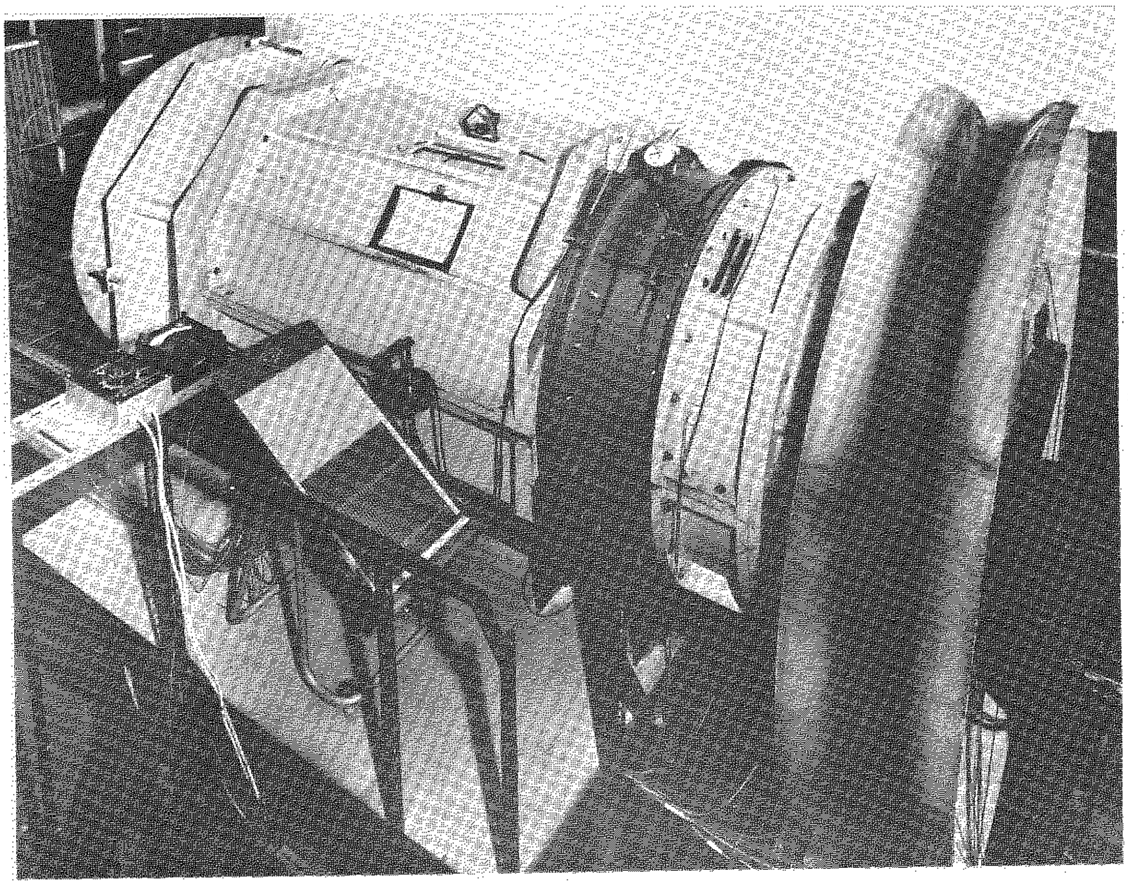

Plate I. General Arrangement of Experimental Apparatus.

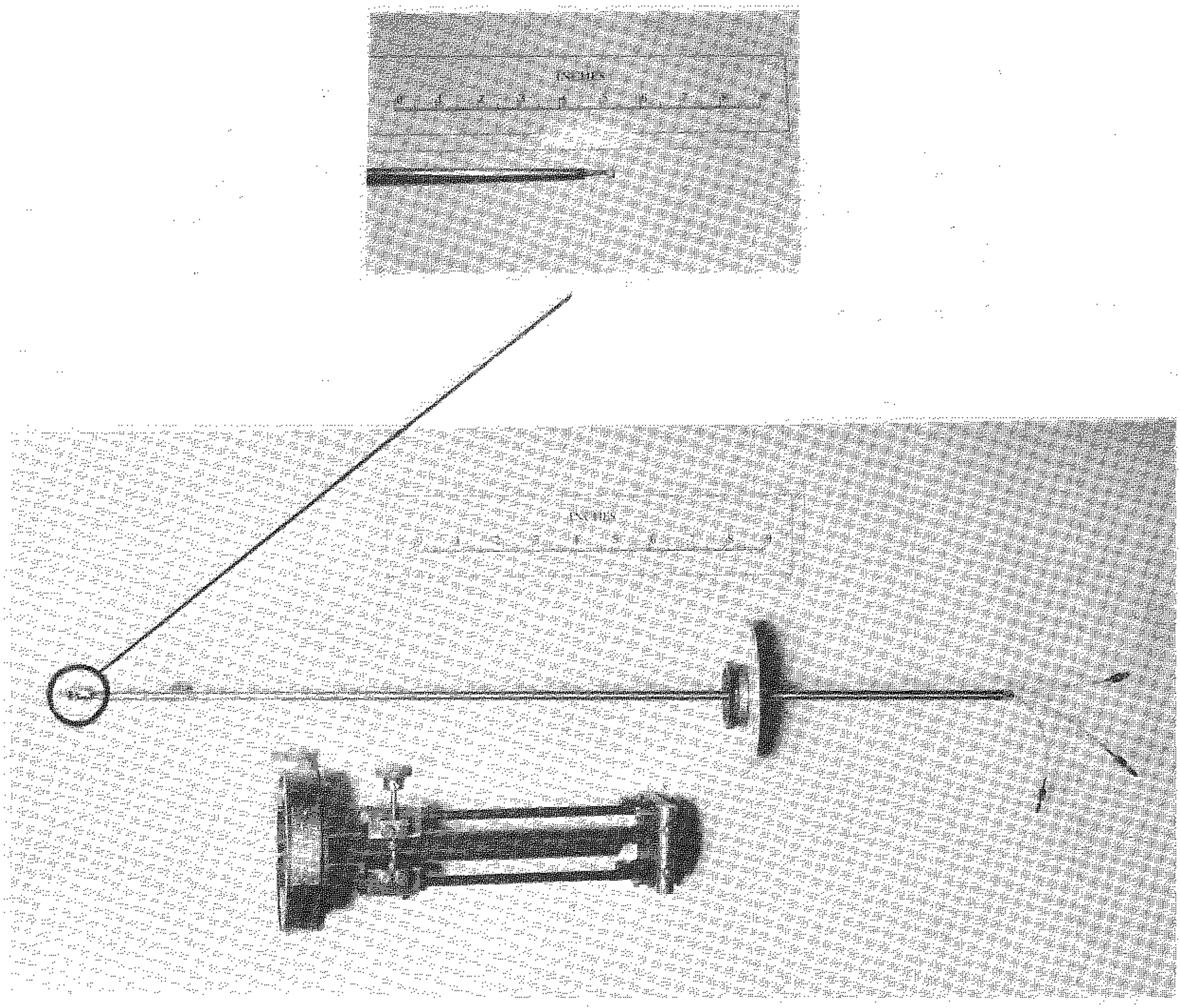

Plate II. The Wedge Instrument and Traversing Mechanism

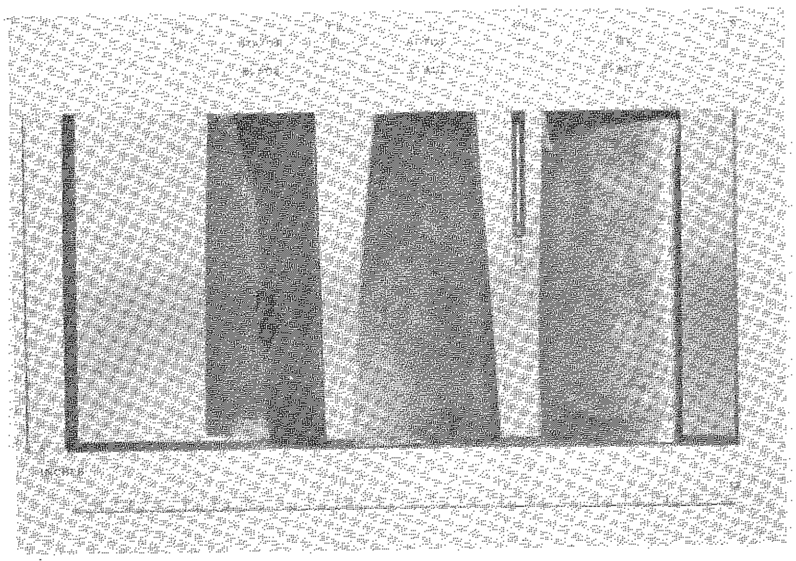

Plate III. Representative set-up of Exponential Blades AR = 2.0

I.S. ≡ Instrument slot

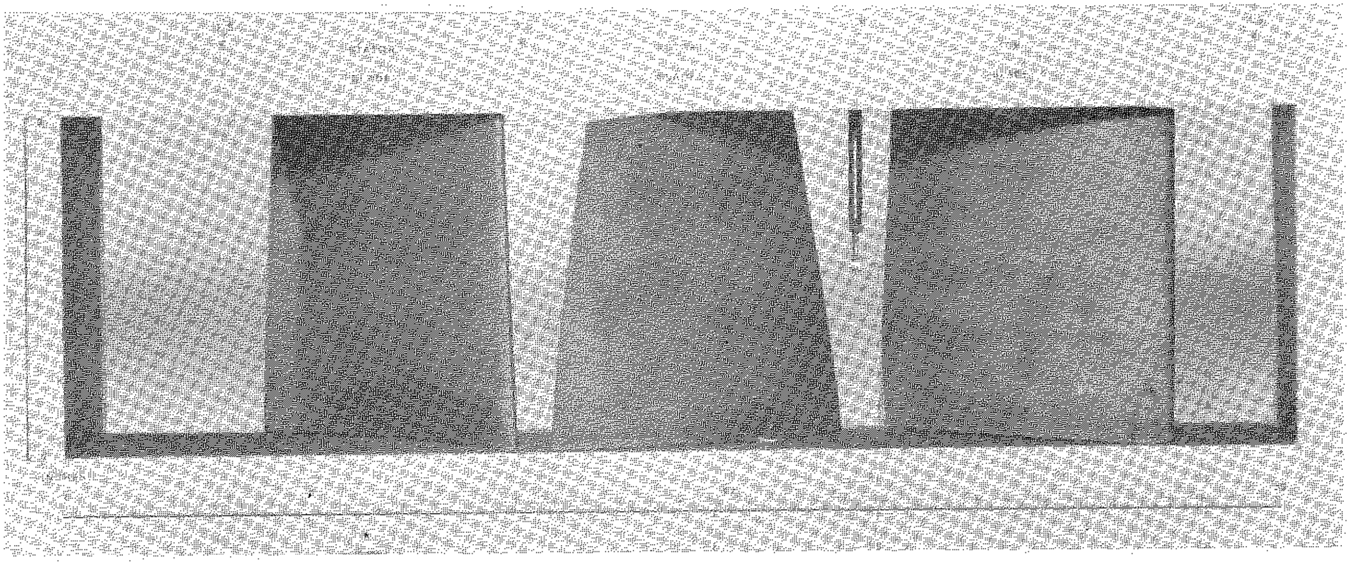

Plate IV. Representative set-up of Exponential Blades AR = 1.0

Produced and published by
HER MAJESTY'S STATIONERY OFFICE
To be purchased from
49 High Holborn, London WC1V 6HB
13a Castle Street, Edinburgh EH2 3AR
109 St Mary Street Cardiff CF1 1JW
Brazennose Street, Manchester M60 8AS
50 Fairfax Street, Bristol BS1 3DE
258 Broad Street Birmingham B1 2HE
80 Chichester Street Belfast BT1 4JY
or through booksellers

Printed in England

SBN 11 470447 3